REPORT DOCUMENTATION PAGE

Form Approved OMB No. 0704-0188

maintaining the data needed, and completing and reviewing the collection of information. Send comments regarding this burden estimate or any other aspect of this collection of information, including suggestions for reducing the burden, to Department of Defense, Washington Headquarters Services, Directorate for Information Operations and Reports (0704-0188), 1215 Jefferson Davis Highway, Suite 1204, Arlington, VA 22202-4302. Respondents should be aware that notwithstanding any other provision of law, no person shall be subject to any penalty for failing to comply with a collection of information if it does not display a currently valid OMB control number.
PLEASE DO NOT RETURN YOUR FORM TO THE ABOVE ADDRESS.

1. REPORT DATE (DD-MM-YYYY)	2. REPORT TYPE	3. DATES COVERED (From – To)
10-10-2001	Final Report	7/14/2000 - 14-Jul-01

4. TITLE AND SUBTITLE

Advanced Modeling for Ductile Behavior of Material Under High Strain Rates and Temperature Using Continuum Mechanics and Solid State Equations

5a. CONTRACT NUMBER
F61775-00-WE029

5b. GRANT NUMBER

5c. PROGRAM ELEMENT NUMBER

6. AUTHOR(S)

Dr. Nicola Bonora

5d. PROJECT NUMBER

5d. TASK NUMBER

5e. WORK UNIT NUMBER

7. PERFORMING ORGANIZATION NAME(S) AND ADDRESS(ES)
University of Cassino
Via G. Di Biasio 43
Cassino 03043
Italy

8. PERFORMING ORGANIZATION REPORT NUMBER

N/A

9. SPONSORING/MONITORING AGENCY NAME(S) AND ADDRESS(ES)

EOARD
PSC 802 BOX 14
FPO 09499-0014

10. SPONSOR/MONITOR'S ACRONYM(S)

11. SPONSOR/MONITOR'S REPORT NUMBER(S)
SPC 00-4029

12. DISTRIBUTION/AVAILABILITY STATEMENT

Approved for public release; distribution is unlimited.

13. SUPPLEMENTARY NOTES

14. ABSTRACT

This report results from a contract tasking University of Cassino as follows: The contractor shall investigate the behavior of ductile metals under high strain rates at various temperatures. The contractor shall produce a new advanced model for predicting ductile failure in metals using continuum mechanics and solid state equations.

20011101 046

15. SUBJECT TERMS
EOARD, Materials, Metals & alloys

16. SECURITY CLASSIFICATION OF:			17. LIMITATION OF ABSTRACT	18. NUMBER OF PAGES	19a. NAME OF RESPONSIBLE PERSON
a. REPORT	b. ABSTRACT	c. THIS PAGE	UL		Charles H. Ward, Maj, USAF
UNCLAS	UNCLAS	UNCLAS		68	19b. TELEPHONE NUMBER (Include area code) +44 (0)20 7514 3154

Standard Form 298 (Rev. 8/98)
Prescribed by ANSI Std. Z39-18

RESEARCH CONTRACT

N° F61775-00-WE029

Advanced Modeling For Ductile Behavior of Materials Under High Strain Rates and Temperature Using Continuum Damage Mechanics and Solid State Equations

FINAL REPORT

TO: E.O.A.R.D., 223/231 MARYLEBONE RD., LONDON NW1 %TH — ENGLAND
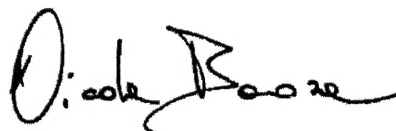
AUTHORS: NICOLA BONORA AND PIETRO PAOLO MILELLA

DIMSAT, DIPARTIMENTO DI MECCANICA, STRUTTURE AMBIENTE E TERRITORIO FACOLTÀ DI INGEGNERIA

UNIVERSITÀ DI CASSINO VIA DI BIASIO 43, 03043 CASSINO (FR), ITALY

JULY, 2001

AQ F02-01-0100

INDEX

STATEMENT

In accordance with Defense Federal Acquisition Regulation 252.227-7036, Declaration of Technical Data Conformity Jan 1997), the contractor, Nicola Bonora – University of Cassino, hereby declares that, to the best is knowledge and belief, the technical data delivered herewith under Contract n°F61775-00-WE029 is complete, accurate and complies with all requirements of the contract.

Date: July 14th 2000

In accordance with the requirements in Federal Acquisition Regulation 52.227-13 Patent Rights- Acquisition by the U.S. Government (Jun 1999):

a) Disclosure of all subject inventions as defined in FAR 52.227-13 have been reported in accordance with this clause
b) I certify that there were no subject inventions to declare as defined in FAR 52.227-13, during the performance of this contract.

Date: July 14th 2001

2

ABSTRACT

The proposed research addresses the issue of advanced fracture design and prediction, in particular ductile fracture of aeronautical materials and structures, using continuum damage mechanics (CDM) that takes into consideration both temperature and strain rate effects on the global material response.

Bonora and Milella (2000) proposed a theoretical framework in order to incorporate strain rate effect, temperature and damage into a simple and effective, physically based, constitutive model. Here, the research work started with the AFOSR research contract n° F61775-99-WE066, is continued addressing the issue of a unified solid state equation (USSE) for any class of metal.

Additionally, the part of the model that deals with ductile damage has been extended in order to incorporate complex load path such as reversal plastic flow occurrence. The model has been validated elaborating a large amount of bare experimental data partially collected in the literature and partially obtained on direct experiment, such as for copper pure metal.

1. INTRODUCTION

For a large number of both civil and military applications, the loading condition are so severe to challenge structures and components well beyond the normal design conditions, forcing the material to respond in the plastic deformation regime. For these cases, structural integrity assessment can not be performed using conventional design procedures that apply under pre-yielding conditions. Even advanced failure assessment methodologies, such as elastic-plastic fracture mechanics, fails to predict ultimate structure resistance when plastic deformation are large and *J-dominance* conditions are no longer guaranteed.

In the last decades a new science, called "damage mechanics", arose. Here, material constitutive response is understood as the result of the concurrent actions of all those reversible and irreversible mechanisms that occurs in the material microstructure when subjected to external loading. Consequently, failure is not longer seen as an abrupt separate event in the deformation history, but it is understood as the end point of the evolution of a damage state. In this framework many models, even though suffering of large number of limitations, have been proposed in the literature showing the potential of the approach.

The fundamental key of damage mechanics is that if the micro-mechanism of failure, for a specific failure process is know, thus it will be possible in theory to predict the occurrence of failure in all materials or structural components, however loaded, in which failure is controlled by the same process.

This statement is particularly important for a large number of practical applications in which structural integrity assessment is jeopardized by geometrical constraint effects, load rates, temperature regimes, etc.

The role of dynamic response of materials is critical for all those applications such as high and hyper velocity impact mechanics, explosion mechanics, etc. The need to have advanced constitutive models is extremely urgent since numerical simulation, that can provide a fundamental insight in the phenomena comprehension and reduction of costs through optimal experimental design, are still today extremely limited in their prediction capabilities as a result of this lacking.

Bonora and Milella (2000) pointed out the possibility to develop a simple and effective constitutive framework, physically based, in order to account for material damage mechanics, strain rate and temperature in material response. Here, the previous work supported by AFOSR SPC F61775-99-WE066, is continued. The objectives of the work are several.

Firstly, the constitutive model for material elastic-plastic response with respect to strain rate and temperature has been extended to a general formulation valid for all classes of metal structure (BCC, FCC, HCP). To this purpose an extensive discussion is dedicated to the model theoretical assessment and parameter identification. Additionally, a very extensive material database has been collected and analysed in order to validate the model prediction capabilities. Additional data on pure copper have been provided

through dedicated experimental program exploring material response in a wide range of strain rates and temperatures.

Parallel to this, ductile damage model has been extended in order to account for complex load path where compression state of stress can occur. This issue, as far as the authors are aware of, has not been addressed in the published literature since now. It is fundamental in all those applications where plastic deformations accumulates both under tensile and compressive state of stress such as soft-spall failure in flying plate impact, where other damage models fail in predicting time and location of failure.
Additional insight on strain rate and temperature effect on damage parameters is also given for a wide range of metals. Damage measurement for pure copper has been also performed.

The model has been implemented in form of user subroutine in a finite element commercial code

2. UNIFIED SOLID STATE EQUATION (USSE)

2.1. BACKGROUND

It is now well recognized that metals with a body-centered cubic (BCC) lattice, like α-iron, ferritic steels, niobium, tantalum etc., have a mechanical behavior strongly dependent on the temperature T and the strain rate $\dot{\varepsilon}$. This, in general, is not observed in metals having a face-centered cubic (FCC) structure, like austenitic steels, nickel, aluminum, copper, silver, etc., that seem not have the same sensitivity to temperature, in particular. Between the two, there are metals with a closely-packed hexagonal lattice (HCP), like titanium and zinc, that do show a dependence of the yield strength on temperature and strain rate, but less pronounced than in BCC materials. It is rather difficult to describe the plastic behavior of all metals through a generalized process that leads to a unified theory. Many attempts have been made in the past to establish what is known as the mechanical equation of the solid state that, like the gas state where pressure and volume are linked with temperature, relates the yield strength σ_y to the temperature T and the strain rate $\dot{\varepsilon}$:

$$\sigma_y = f(\varepsilon, \dot{\varepsilon}, T) \tag{2.1.1}$$

Zener and Hollomon (1944), Manjoine (1944), Cottrell (1948, '49, '53, '57 and '58), Hollomon (1947), Yokobori (1953), Orowan (1954), Seeger (1954 and 1955), Campbell (1953, 1959), Conrad (1960, 1961), Conrad et al. (1962), Petch (1953, 1957 and 1964) and others, have tried to derive that equation through an empirical or physical approach, based on experiments, or a physical one based on either the activation energy concept or dislocation models. Often, the solid state or constitutive equations proposed were not consistent at all, but in general, it has been found an exponential dependence of the yield strength σ_y on temperature and an equivalence between temperature and strain rate. This latter aspect, in particular, is well shown by the Zener and Hollomon equation:

$$\sigma_y = f(\dot{\varepsilon} \cdot e^{Q/RT}) \tag{2.1.2}$$

where Q is the so-called activation energy and R the universal gas constant. More recently, Hoge and Mukherjee (1977), Johnson and Cook (1983), Johnson et al. (1983), Klopp et al. (1985), Follansbee (1986), Zerilly-Armstrong (1987, 1990 and 1992), Follansbee and Kocks (1988) and Nemat-Nasser et al. (1998, 1998, 1996) have addressed the issue and developed empirical or physically-based constitutive equations. The Johnson and Cook (JC) model, in particular, has enjoyed much success because of its simplicity. The JC model is an empirical five parameter constitutive equation that takes the form:

$$\sigma_{flow} = \left(A + B\varepsilon^n\right) \cdot \left(1 + C \cdot ln\dot{\varepsilon}^*\right) \cdot \left(1 - T^{*m}\right) \tag{2.1.3}$$

where s_{flow} and e are the von Mises flow stress and the equivalent plastic strain,

respectively, $\dot{\varepsilon}^* = \dot{\varepsilon}/\dot{\varepsilon}_o$ is a dimensionless strain rate with $\dot{\varepsilon}_o$ equal to 1.0 s^{-1}, and T^* is the homologous temperature defined as:

$$T^* = \frac{T-T_r}{T_m-T_r}$$

(2.1.4)

where T_r is a reference temperature (normally the room temperature RT) and T_m the melting temperature of the material. A, B, n, C and m are the five material constants. In Eq. (2.1.3), the first set in brackets gives the dependence of the flow stress on strain, while the second and third one provide the dependence on strain rate and temperature, respectively. At variance, the Zerilli-Armstrong constitutive equation is a physically based model. It is a three parameter model that has a very good capability to fit experimental results. It is based on thermally activated dislocation motion focusing on the relevant difference between BCC and FCC metal response, as it will be shown. Accordingly, it takes a different form for BCC and FCC lattice metals:

$$BCC: \quad \sigma_y = C_1 \exp\left(-C_3 T + C_4 T \ln \dot{\varepsilon}\right)$$
$$FCC: \quad \sigma_{flow} = C_2 \varepsilon^{1/2} \exp\left(-C_3 T + C_4 T \ln \dot{\varepsilon}\right)$$

(2.1.5)

The purpose of this research is to present a unified constitutive equation, or unified mechanical equation of the solid state (USSE), valid for all metals.

2.2. SUMMARY OF THE PREVIOUS RESEARCH

The current research deals with the material response, typically the yield strength σ_y, to temperature and strain rate. It is the continuation of the previous research contract N. F61775-99-WE066 from AFOSR, where a constitutive equation was inferred for BCC steels in the low and high strain rate domain, as well. In particular for the low strain rate domain where the Peierls-Nabarro barrier is the dominant mechanism that opposes dislocations motion, the equation of the solid state (SSE) takes the form:

$$\sigma_y = C \cdot \left(e^{D/T} \dot{\varepsilon}^{E/T}\right)$$

(2.2.1)

Where C, D and E are material characteristics. It was shown that, independently of the strain rate $\dot{\varepsilon}$ applied, the trend of the natural logarithm of the yield strength $ln(\sigma_y)$ versus $1/T$ is linear and all the lines relative to the different strain rates, converge towards a common point. This is shown in figures 2.2.1, 2.2.2 and 2.2.3 for carbon steels A 533 B and A 537 Cl1 and for niobium, respectively. Niobium is not a steel, yet it has a BCC structure. The definition and extension of the low strain rate domain depends on the particular metal or alloy and its sensitivity to strain rate. For carbon steel, the low strain rate domain is that below 1000 s^{-1}. For niobium, 0.15 s^{-1} is already a high $\dot{\varepsilon}$. Constant C in Eq. (2.5) is given by:
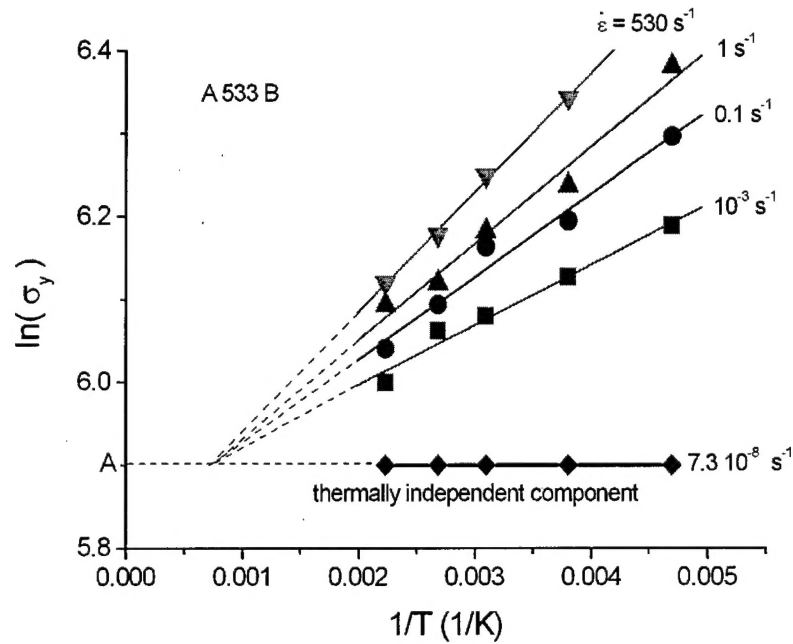
$$C = e^A$$

(2.2.2)

Figure 2.2.1 – Trend of ln(σ_y) versus 1/T observed on A 533 B steel at various strain rates. The lines converge towards a common point, whose ordinate A provides the value of the athermal component of the yield strength.
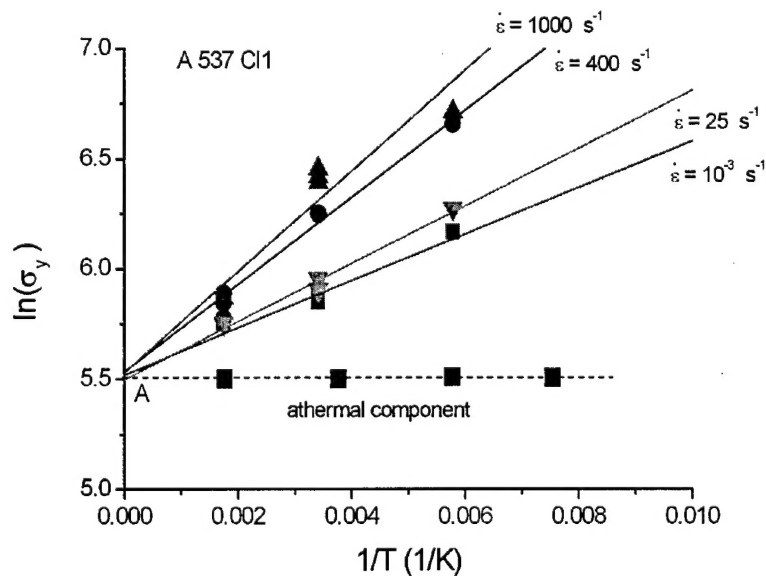

Figure 2.2.2 – Trend of ln(σ_y) vs 1/T observed on A 537 Cl1 steel at various strain rates. The lines converge towards a common point that provides the value of the athermal component of the yield strength.
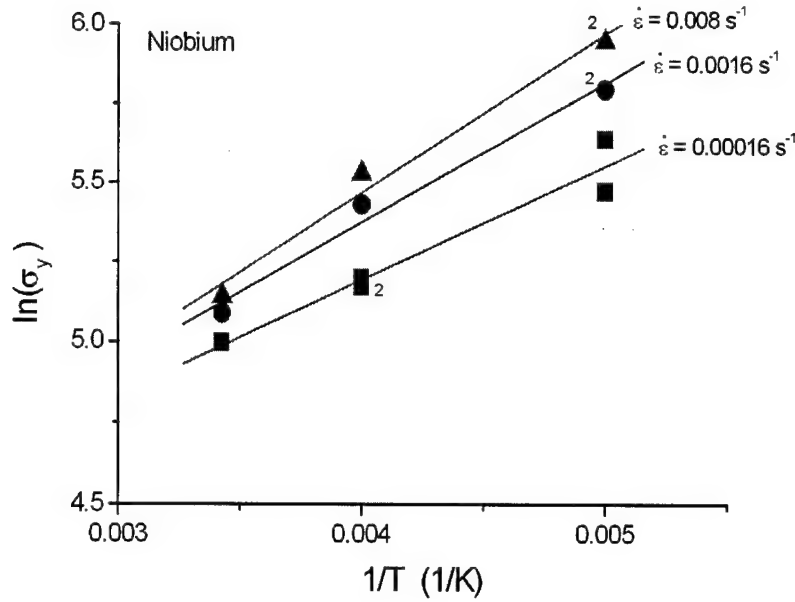
Figure 2.2.3 – Trend of ln(σ_y) vs 1/T observed on niobium at various strain rates. The lines converge towards a common point that provides the value of the athermal component of the yield strength.

where A is the ordinate of the merging point, see Fig. 2.2.1 and Fig. 2.2.2, that represents the athermal component of the yield strength, while D and E are the coefficient of the equation:

$$B = D \cdot ln\dot{\varepsilon} + E \qquad (2.2.3)$$

that describes the linear dependence of the slopes B of the various lines of Figures 2.2.1, 2.2.2 and 2.2.3 as a function of the natural logarithm of the strain rate, $ln\dot{\varepsilon}$. This is shown in Figure 2.2.4, 2.2.5 and 2.2.6 for A 533 B, A 537 and niobium, respectively. Knowing D and E, by equating the right term of Eq. 2.2.3 to zero ($B = 0$) the value of the strain rate $\dot{\varepsilon}$ at which temperature has no more effect on the yield strength is obtained. For the metals considered in Figures 2.2.1, 2.2.2 and 2.2.3 this limiting strain rate is of the order of 10^{-8} s^{-1}. Figures 2.1.1, 2.1.2 and 2.1.3, show that as temperature increases, the responses of the material at different strain rates come closer and closer as if temperature were *washing-out* the strain rate effect. The opposite happens at high strain rates, where the material is more sensitive at high temperatures, and the mechanical responses get closer and closer as temperature decreases. This can be seen for A 533 B and A 508 Cl3 steels in Figures 2.2.7 and 2.2.8 and for niobium in figure 2.2.9. This is because, as it will be described in the next paragraphs, at higher temperature and strain rates the Peierls-Nabarro barrier on moving dislocation is less sensitive to temperature and is replaced by solute atoms, phonon-drag and electron-drag resistance as primary effect. (Follansbee et al., 1982; Regazzoni et al., 1992; Zerilli and Armstrong, 1992; Kapoor et al., 1999).
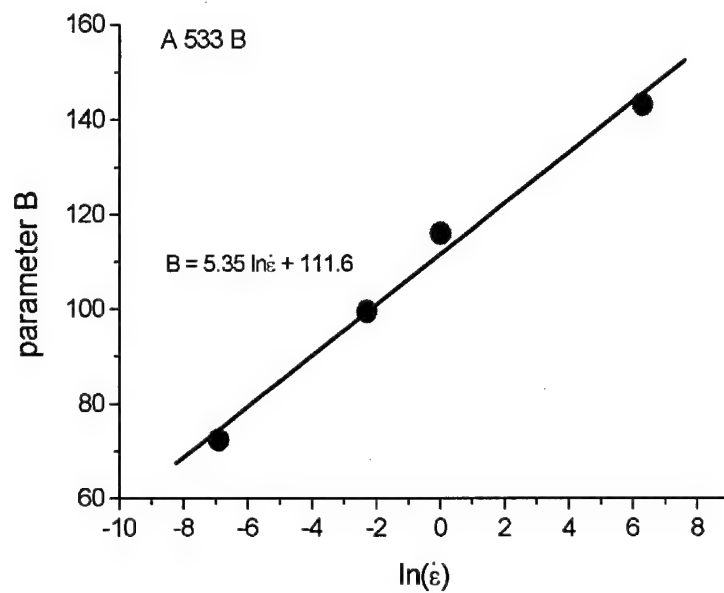
Figure 2.2.4 – Linear trend of the slopes of the four lines of Fig. 2.1.1 versus ln $\dot{\varepsilon}$.
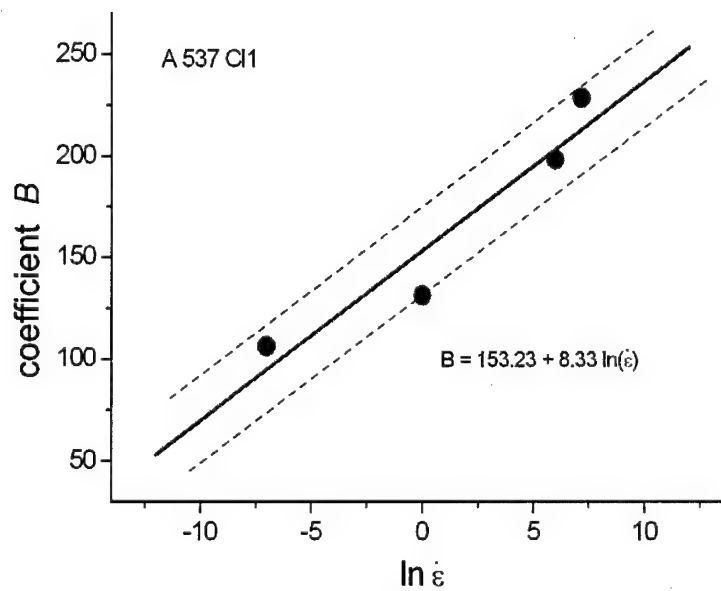

Figure 2.2.5 – Trend of the slopes of the four lines of Fig. 2.1.2 versus ln $\dot{\varepsilon}$.
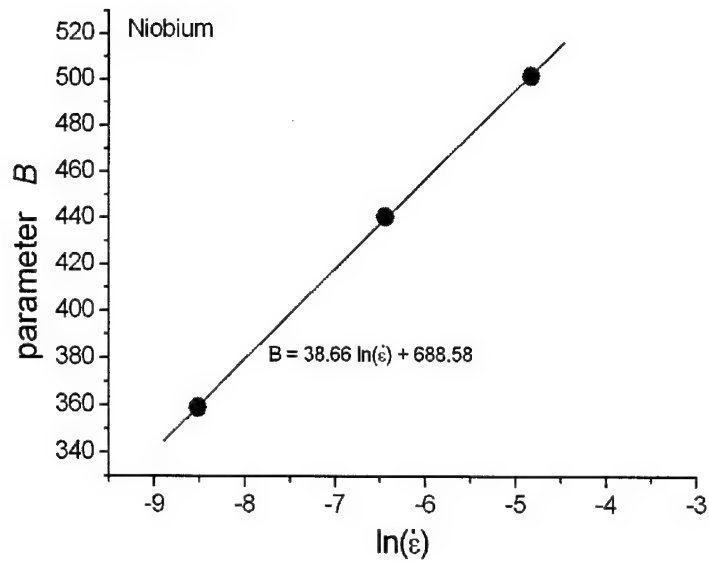
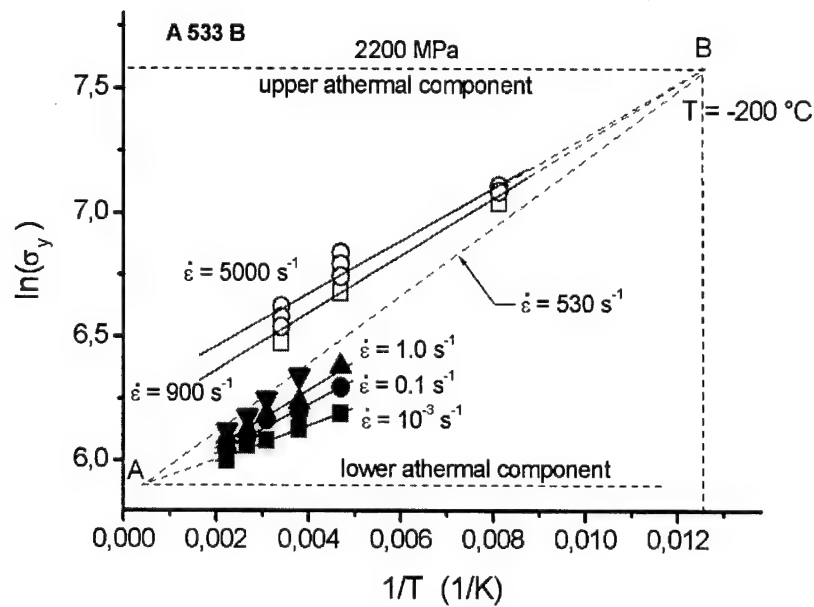*Figure 2.2.6 – Linear trend of the slopes of the lines of Fig. 2.2.3 versus ln $\dot{\varepsilon}$.*

Figure 2.2.7 – High and low strain rate dependence of the lnσ_y vs 1/T in A 533 B steel.
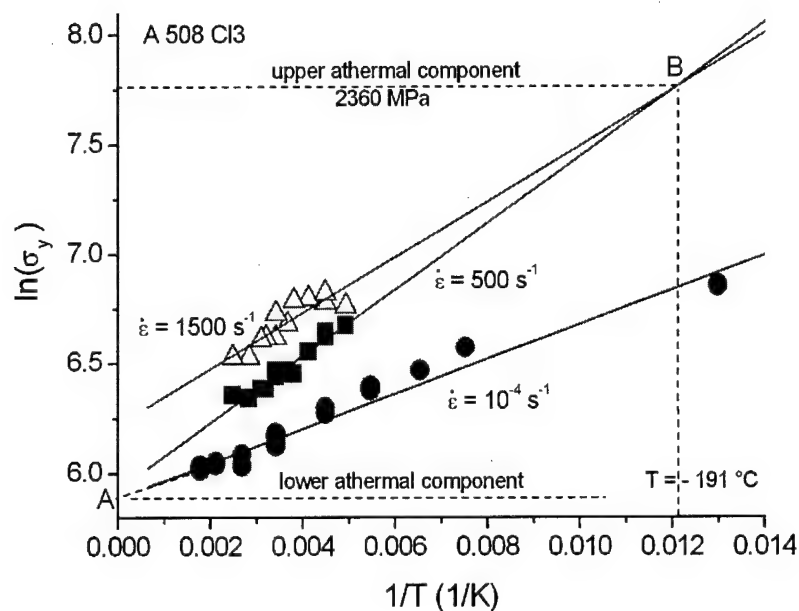
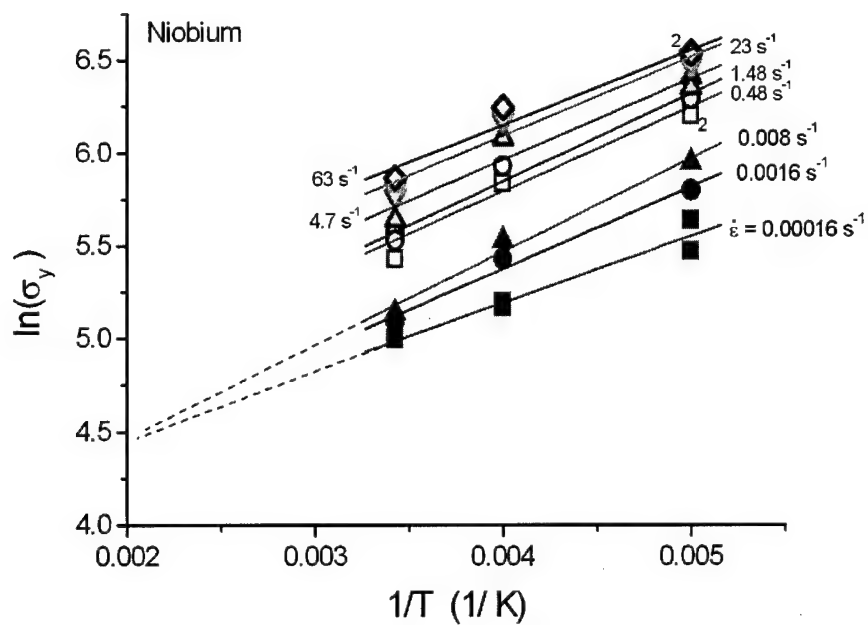*Figure 2.2.8 – High and low strain rate dependence of the lnσ_y vs 1/T in A 508 B steel.*

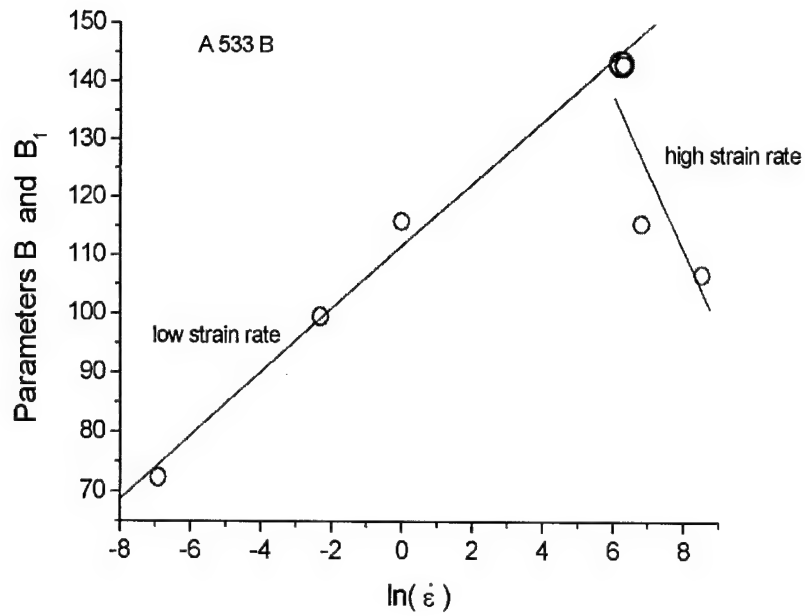*Figure 2.2.9 – High and low strain rate dependence of the lnσ_y vs 1/T in niobium.*

12

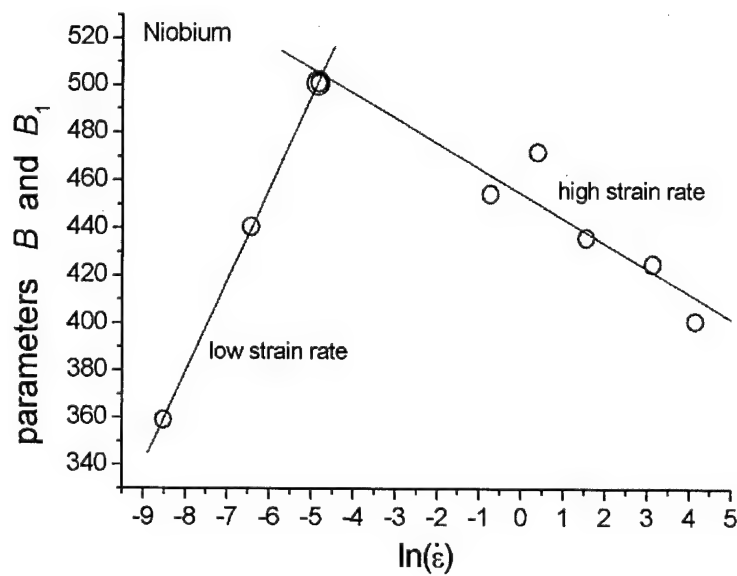*Figure 2.2.10 – Low and high strain rate trend of parameters B and B₁ for A 533 B steel.*

Figure 2.2.11 – Low and high strain rate trend of parameters B and B₁ for niobium.

For the new field of strain rates investigated, over 500 s^{-1}, the new SSE is:

$$\sigma_y = C_1 \left(e^{D_1/T} \frac{\dot{\varepsilon}^{E_1/T}}{\dot{\varepsilon}^{E_1/T_{min}}} \right) \qquad (2.2.4)$$

where C_1, D_1 and E_1 are material characteristics and T_{min} is the temperature at which the lines converge (point B). It is particularly interesting to observe the trend of the parameter B, already shown in Figures 2.2.4, 2.2.5 and 2.2.6 for the low strain rate regime, at high strain rates $\dot{\varepsilon}$. This trend is presented in Figure 2.2.10 for A 533 B and in Figure 2.2.11 for niobium, respectively. The new parameter has been named B_1. Its equation, for A 533 B, is:

$$B_1 = 219 - 13.5 \cdot ln(\dot{\varepsilon}) \qquad (2.2.5)$$

and for niobium:

$$B_1 = 454 - 11 \cdot ln(\dot{\varepsilon}) \qquad (2.2.6)$$

2.3. THE EFFECT OF TEMPERATURE ON MOVING DISLOCATIONS

To deform a metal beyond the elastic limit or yield strength σ_y, means to activate and move its dislocations through the crystal. Dislocations encounter obstacles as they move through the lattice. Figure 2.3.1 is a simple schematic of some of these obstacles, probably the most common ones: solute atoms, vacancies, clusters, inclusions, grain boundary, precipitates and so on. Inclusions themselves can provide a formidable
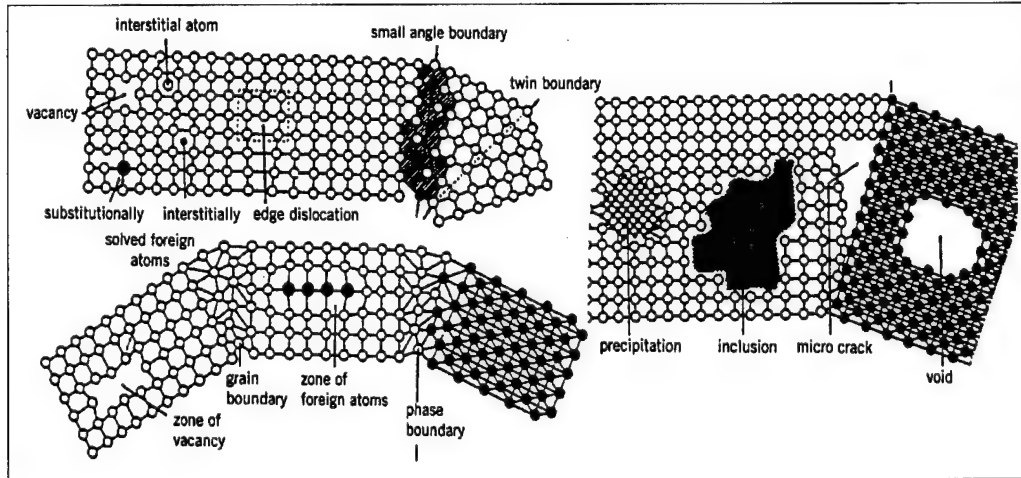

Figure 2.3.1 – Schematic of different types of defect in crystalline materials (Vohringer, fig. 9, p.40, 1989).

barrier as they multiply and create the so called *forests* of dislocations. Some of these, also called long-range obstacles, are due to the structure of the material and cannot be

14

overcome introducing thermal energy into the crystal. Therefore they contribute to the yield strength with a component that is non-thermally activated. Others, on the contrary, can be overcome by thermal energy. These last are normally called short-range barriers. We can, therefore, consider the yield strength of a material σ_y as been made of two components, one *athermal* σ_{at} (long-range component) and the other σ_{ta} *thermally activated* (short-range component):

$$\sigma_y \;=\; \sigma_{at}(structure) \;+\; \sigma_{ta}(T,\dot{\varepsilon},structure) \tag{2.3.1}$$

Probably, a more refined way to express the yield strength is to consider the resistance to dislocation motion as composed of three terms:

$$\sigma_y \;=\; \sigma_{at}(structure) \;+\; \sigma_{vd}(structure) \;+\; \sigma_{ta}(T,\dot{\varepsilon},structure) \tag{2.3.2}$$

where s_{vd} is a long range component due to a viscous-drag resistance exerted by phonon and electrons, as it will be described later. It is worth noting that the thermally activated component σ_{ta} in eq. (2.3.1) has been written as a function of both temperature T and strain rate $\dot{\varepsilon}$, since, as it will be described later, the strain rate has a direct effect on the yield strength, as it can reduce the actual capability of temperature to provide thermal energy to overcome short range barriers. The most important short-range obstacle in BCC lattice metals is the so-called Peierls-Nabarro barrier. This barrier generates the force holding a dislocation in its low-energy position in the lattice, as schematically shown in Figure 2.3.2. The barrier is the consequence of the stress field set up around the dislocation as results of its presence. As dislocation passes from stage a to c it moves through the unstable high energy stage b, which actually means that the dislocation shall overcome a typical energy barrier of the type shown in Figure 2.3.2.
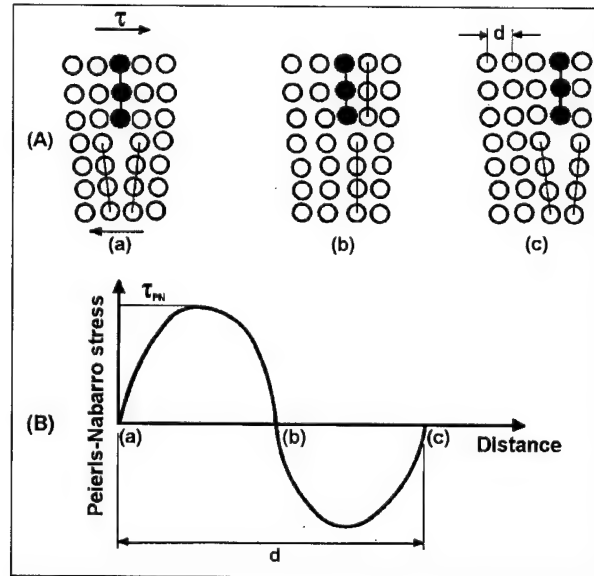

Figure 2.3.2 – (A) movement of dislocation from one equilibrium position(a) to the next (c); (B) Peierls-Nabarro stress vs. distance.

15

The wavelength of this barrier is equal to the periodicity d of the lattice. Effectively, Zerilli and Armstrong (1987, 1992) observing the different behavior shown by BCC and FCC metals, where the BCC structure has a much higher sensitivity to temperature, concluded that overcoming the Peierls-Nabarro barriers was the main thermal activation mechanism for BCC metals. The effect of temperature is also shown in Figure 2.3.3.
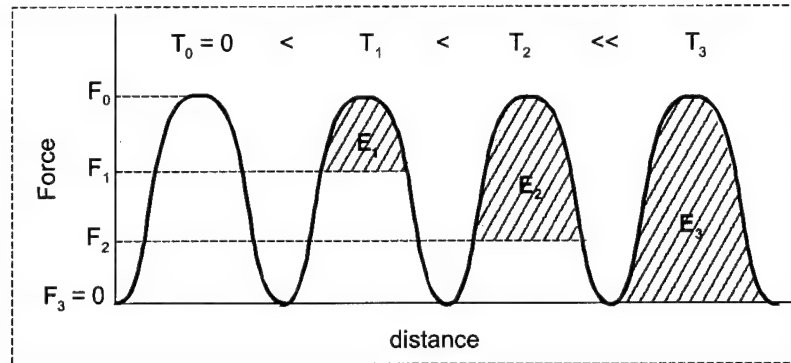

Figure 2.3.3 – Schematic of a Peierls-Nabarro barrier and the relative force F_i that must be applied at different temperatures T_i to move a dislocation.

By increasing the temperature, $T_3 >> T_2 > T_1$, we introduce into the system more and more thermal energy, $E_3 >> E_2 > E_1$, that fills the barrier, whose effective height is reduced and, therefore, the relative force F_i to overcome the barrier and move dislocations is also reduced. This temperature dependent obstacle to the dislocation motion can be also seen in terms of drag stress exerted by the so-called Cottrell's atmosphere. As already said, BCC materials present a yield strength that has a component thermally activated, while FCC ones do not. This difference can be ascribed to the size of dislocations, i.e., to the distance over which the additional plane of atoms deforms the lattice in which it is inserted like a wedge. In this distorted area of the crystal, interstitial atoms, always present in solid solution, like carbon, nitrogen and oxygen, migrate under the wedging pressure exerted by the dislocation. In particular, these atoms will move from the compression side, directly above the dislocation line where the crystal shrinks, to the traction one below the edge, where the lattice is expanded and the tensile stress *attracts* them, creating what is known as the *Cottrell's atmosphere*. Wide dislocations have diluted atmospheres, since the specific distortion (distortion per unit length) of the lattice is negligible, with weak strain and stress fields attracting interstitial atoms. On the contrary, narrow dislocations, where the *disturb* to the lattice is very localized and the stress field is intense, are characterized by atmospheres of high concentration, well over that of the solid solution that surrounds them, especially at lower temperatures. To plastically deform a metal, i.e., to pass its yield point, dislocations must be displaced across the lattice and by doing so, also their atmosphere of interstitial atoms shall be moved. This cloud of atoms, that has to follow each dislocation, will not move freely. As a result, a drag-force is generated that opposes the motion. We can say that the higher the concentration of the Cottrell's atmosphere, with respect to that of the lattice in which it has to move, the greater this force and, therefore, the larger the component of the yield strength produced by that effect. We can envisage a variation of the

concentration of the Cottrell's atmosphere with the size of the dislocations that characterize a particular metal or alloy. The drag force will change accordingly and therefore also its effect on the yield strength. FCC metals have wide dislocations and their atmospheres are, therefore, diluted with a marginal effect on the yield stress. At variance, BCC crystals have narrow dislocations with concentrated atmospheres that oppose their motion, resulting in a sharp yield point. Figure 2.3.4 is a schematic of narrow and large dislocation, respectively. An increase of temperature will introduce
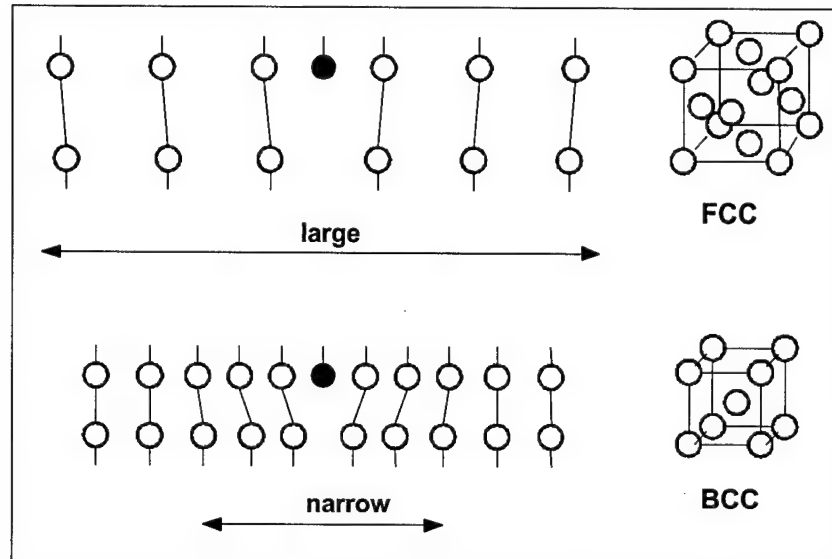

Figure 2.3.4 – Schematic of a large dislocation, typical of BCC lattice, and a narrow one, typical of FCC crystals.

new energy into the system that will allow a certain migration of interstitial atoms from the atmosphere, where they are kept together, towards the lattice. This will determine a dilution of its concentration. At the same time, some precipitates, in particular carbides, will release their non-metal atoms that will enter into solid solution, since temperature enhances solubility of interstitial atoms, so that the lattice concentration will increase. The overall effect will be a net reduction in the unbalance between the Cottrell's atmosphere and the solid solution concentration. This will result in a reduction of the drag-stress that will favor the displacement of dislocations under the action of shear stresses and, therefore, will produce a decrease of the yield strength. By further increasing the temperature the two concentrations come closer and closer, lowering more and more the thermally activated component of the yield strength and, eventually, at a sufficiently high temperature, they will become almost equal. At this time, we can say that dislocation atmospheres no longer exist. Now, dislocations will not distinguish any more between atoms internal and external to the atmosphere, and will move in the lattice exchanging continuously their interstitial atoms with those of the lattice. At this point, the thermal component of the yield strength due to the Cottrell's atmosphere σ_{Ct} is vanished. Now, moving dislocations will encounter only long-range barriers due to the structure of the material, that cannot be overcome by thermal energy and represent the non-thermally activated component of the yield strength. Typical are the viscous-

drag mechanisms exerted by the interaction of dislocations with thermal vibrations (phonon viscosity) and electrons (electron viscosity) (Gorman et al. 1969, Granato, 1973). For BCC metals long range barriers are the stress field of dislocation forests and grain boundary. The opposite will happen if temperature is reduced. In this case, there will be a massive precipitation of interstitial atoms, again mainly in the form of carbides that will abandon the lattice diluting the solid solution. Some of them will also re-flourish the atmospheres that may not suffer any loss of atoms, since these are *frozen* in their position. This process will enhance the difference between the two concentrations and, therefore, will augment both the force anchoring dislocations and the yield strength. This component of the yield strength that is thermally activated is not present, as experience shows, in FCC structures probably because, as said, the Cottrell's atmosphere is already diluted at any temperature at a value that approaches that of the solid solution. We can say that, in general, the more those two concentrations differ the higher the resulting drag stress and, therefore, the component σ_{Ct}. To visualize the effect of temperature just mentioned, it can be useful to look at the carbon solubility in the lattice. Carbon certainly provides the most abundant source of foreign atoms that enter into solid solution and is characterized by a great mobility. Carbon solubility in ferrite can be expressed by the following relation (Wert, 1950):

$$C(\%) = 2.55 \cdot e^{-9700/RT} \qquad (2.3.3)$$

where C(%) is the concentration in percent in weight of carbon, R the universal gas constant, equal to 2 cal/mole K, and T the temperature, in degree Kelvin. At the eutectoid temperature, ~723 °C, the carbon concentration resulting from Eq. (2.3.3) is about 0.02 %. Already at ambient temperature (RT) it becomes $2 \cdot 10^{-7}$. This means that by lowering the temperature of about 700 °C, from 723 °C to RT, the Cottrell's atmosphere will face an environment where the concentration of interstitial carbon atoms declined by a factor 10^5. This is a tremendous reduction that will be felt by the material through a sharp increase of the yield strength. Because of the exponential nature of Eq. (2.3.3), a further decrease of temperature, this time of only 125 °C, from RT to −100 °C, will result in an even greater reduction of concentration by a factor 10^6, approximately. In this second temperature drop, we shall then expect an even larger increase of the yield strength, as experience is actually indicating. We will associate, then, the variation, $d\sigma_y$, of the yield strength from its current value σ_y, to the corresponding variation $d\lambda$ of the ratio of the concentration of the Cottrell's atmosphere n_C, to that n_s of the solid solution, relative to its current value $\lambda(T)=n_C/n_s$:

$$\frac{d\sigma_y}{\sigma_y} = \frac{d\lambda}{\lambda(T)} \qquad (2.3.4)$$

We can express the global concentration n_s of all foreign atoms, carbon, nitrogen, oxygen etc., in solid solution in a form like that of Eq. (2.3.3), relative only to carbon:

$$n_s = a \cdot e^{-\frac{b}{RT}} \qquad (2.3.5)$$

where a and b are material characteristics. Also the concentration $n_C > n_s$ of the Cottrell's atmosphere will be expressed in the same fashion:

18

$$n_C = c \cdot e^{\frac{d}{RT}} \tag{2.3.6}$$

with c and d material characteristics. This time, the exponent is positive, since it is supposed, at the moment, that the concentration of the Cottrell's atmosphere decreases with temperature. The ratio $\lambda(n)$ will then become:

$$\lambda(T) = \frac{n_C}{n_s} = f \cdot e^{\frac{g}{RT}} \tag{2.3.7}$$

with $f=c/a$ and $g=b+d$. Integrating Eq. (2.3.4) between a reference temperatures T_0 and T:

$$\int_{T_0}^{T} \frac{d\sigma_y}{\sigma_y} = \int_{T_0}^{T} \frac{d\lambda}{\lambda} \tag{2.3.8}$$

yields:

$$\ln \sigma_y(T_0) - \ln \sigma_y(T) = \ln \lambda(T_0) - \ln \lambda(T);$$

$$\ln \sigma_y(T_0) - \ln \sigma_y(T) = \frac{g}{RT_0} - \frac{g}{RT}; \tag{2.3.9}$$

$$\ln \sigma_y(T) = \frac{g}{RT} + \ln \sigma_y(T_0) - \frac{g}{RT_0}$$

The last of Eqn. (2.3.9) can be written as:

$$\ln \sigma_y(T) = \frac{B}{T} + A \tag{2.3.10}$$

with A and B constants characteristic of the material:

$$A = \left[\ln \sigma_y(T_0) - \frac{g}{RT_0} \right] \; ; \; B = \frac{g}{R} \tag{2.3.11}$$

that, as we will see, can be easily determined experimentally. Eq. (2.3.10) provides the base for the definition of the mechanical equation of the solid state. In its explicit form it relates the yield strength to the temperature:

$$\sigma_y(T) = C \cdot e^{\frac{B}{T}} \tag{2.3.12}$$

where:

$$C = e^A = \sigma_y(T_0) \cdot e^{-\frac{g}{RT_0}} \tag{2.3.13}$$

It is worth noting the similarity between Eq. (2.3.12) derived from a dislocation model and Eq. (2.1.2) based on the activation energy.

2.4. THE EFFECT OF STRAIN RATE ON MOVING DISLOCATIONS

We have considered, in the previous paragraph, the effect of temperature on dislocation motion. This effect, however, cannot be separated from that exerted by the dynamic application of a deformation, i.e., the strain rate. Let's look at the short-range obstacles already considered. We have shown that the Cottrell's atmosphere has an impact on the force required to move a dislocation. Dislocations move by a slip mechanism, whereas the atmosphere of interstitial atoms moves by diffusion, which is a completely different mechanism. Therefore, the resulting drag-stress is controlled by the dislocation velocity, that depends on the strain rate, and the diffusion rate of the interstitials, that depends on the temperature. This creates a direct interdependence between strain rate and temperature. At extremely low strain rates the dislocation velocity may be comparable to the diffusion rate and dislocations may move along with their atmospheres without any drag-stress. We have seen that for steels, as well as for niobium, this strain rate is of the order of 10^{-8} s^{-1}. At this strain rate, temperature has no effect on moving dislocations and the yield strength reduces to the athermal component. At extremely high velocity the dislocation passes through the solute atoms at such a fast rate that there is insufficient time for the atoms to follow it: the atmosphere is left behind and lost. Also under this conditions an atmosphere of solute atoms should not exist and the dislocations should move without any thermal effect. This has been shown to be the upper athermal component of the yield strength (see Figs. 2.2.7 and 2.2.8). In between these two extreme conditions there must be the abovementioned interdependence between temperature and strain rate. Interesting, from the point of view of dislocation velocity-temperature interaction, is Figure 2.4.1 (Meyers and Murr, 1981). The figure refers to nickel, but the concepts are generic in nature. Three different regions are defined, identifying three different mechanisms governing plastic deformation: REGION I refers to the thermally activated dislocation motion, REGION II to the phonon-drag and electron-drag resistance non thermally activated and REGION III to relativistic effects where dislocation velocity approaches that of shear waves. Eq. (2.2.1) is actually showing this interdependence and how temperature is washing out the strain rate effect. This actually means that the traditional approach to separate the yield strength of a material into two or three additive components, Eq. (2.3.1) and Eq. (2.3.2) respectively, is a too simple one. The JC constitutive equation (2.1.3) or the Milella equation (2.2.1) clearly show this interdependence that is not simply additive, so that some concerns may arise about the Zerilly-Armstrong equation, Eq. (2.1.5), that still retains this concept. Returning to the Peierls-Nabarro barrier, shown in Fig. 2.3.3, we can use a statistical mechanics approach, and say that at equilibrium the probability P to get a thermal fluctuation whose amplitude is greater than E is given by:
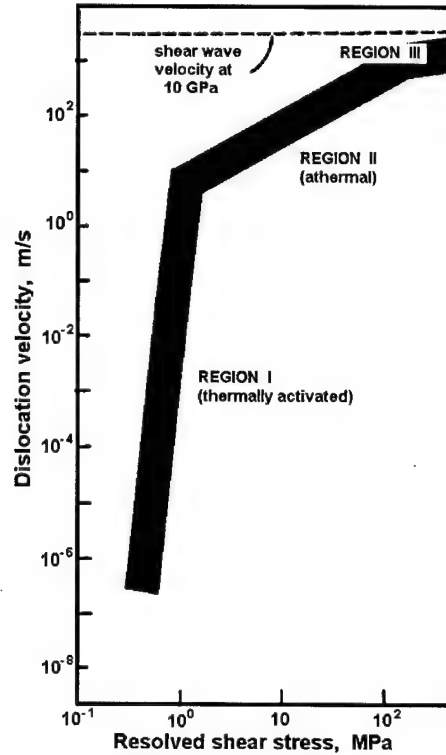
Figure 2.4.1 – Schematic representation of the three regions in nickel where different mechanisms are active (Meyers and Murr, 1981).

$$P \; = \; exp\left(-\frac{E}{kT}\right) \tag{2.4.1}$$

where k is the Boltzman's constant. Eq. (2.4.1) leads to a yield strength exponential dependence on temperature, as described by eq. (2.1.2). We shall assume that a dislocation will overcome the barrier if the energy E is equal or higher than that of the barrier. Let's try to evaluate the strain rate effect on that probability. For convenience, let's switch from probability to frequency and say that the frequency ω with which a dislocation overcomes the obstacle is given by:

$$\omega \; = \; \omega_o \, exp\left(-\frac{E}{kT}\right) \tag{2.4.2}$$

where ω_o is the vibrational frequency of a dislocation. Kocks et al. (1975) discussing the subject concluded that ω_o should be $\sim 10^{11}$ s^{-1}, i.e., about 100 times lower than the vibrational frequency of atoms. The inverse of Eq. (2.4.2) is the average time needed to overcome an obstacle:

$$t = \frac{1}{\omega_o} \exp\left(\frac{E}{kT}\right) \qquad (2.4.3)$$

The strain rate $\dot{\varepsilon} = d\varepsilon/dt$ can be expressed as:

$$\dot{\varepsilon} = \frac{\rho b v}{M} \qquad (2.4.4)$$

where ρ is the dislocation density, b the Burger vector, v the dislocation velocity and M a so called orientation factor equal to 3.1 for FCC crystals and 2.75 for BCC ones. Hence, expressing v as l/t, where l is the distance between obstacles and t the time given by Eq. (2.4.3) we get:

$$\dot{\varepsilon} = \frac{\omega_o \rho b l}{M} \exp\left(-\frac{E}{kT}\right)$$
$$= \dot{\varepsilon}_o \exp\left(-\frac{E}{kT}\right) \qquad (2.4.5)$$

with:

$$\dot{\varepsilon}_o = \frac{\omega_o \rho b l}{M} \qquad (2.4.6)$$

By solving Eq. (2.4.5) in terms of E we get the explicit form for the energy E:

$$E = kT \cdot \ln\left(\frac{\dot{\varepsilon}_o}{\dot{\varepsilon}}\right) \qquad (2.4.7)$$

Eq. (2.4.7) states that the capability to overcome a barrier increases with temperature T and decreases with increasing strain rate $\dot{\varepsilon}$. It is the foundation for constitutive equations based on thermally activated dislocation motion, such as the Zerilly-Armstrong one, Eq. (2.1.5). But it also contains another important information. In fact, as the applied strain rate reaches the value of $\dot{\varepsilon}_o$ the relative energy available to overcome the barrier becomes zero, no matter what the temperature is. In other words, there will be a limiting strain rate at which the response of the material is thermally independent. We can calculate the value of this limiting strain rate. It is given by Eq. (2.4.6). For a mild steel, considering that ω_o is 10^{10}-10^{11} s^{-1}, ρ is about 10^{12} m^{-2}, $b = 3\cdot10^{-8}$ m and $l \sim \rho^{-1/2} = 10^{-6}$ m, we get:

$$\dot{\varepsilon}_{limit} = \dot{\varepsilon}_o \approx 10^9 - 10^8 \quad s^{-1} \qquad (2.4.8)$$

This is the strain rate at which the upper athermal component of the yield stress should be reached. Looking at Fig. 2.2.9 and Eq. (2.2.9) the value of this limiting strain rate $\dot{\varepsilon}_{limit}$ is obtained equating to zero Eq. (2.2.9), $B_l = 0$, $\dot{\varepsilon}_{limit} = 10^7$ s^{-1}. We can conclude that as the strain rate increases, the effect of temperature decreases passing from a situation were the temperature is washing out the strain rate effect (low applied

strain rate) to a new one in which the strain rate will wash-out the temperature effect. As already mentioned, Figs. 2.2.7 and 2.2.8 show this transition at a strain rate over 500 s^{-1}. The actual value of this transition strain rate, however, depends on the material and its structure. For instance, 0.1 s^{-1} is already a high strain rate for niobium. It must be kept in mind that by increasing the strain rate another effect takes place. This is the already mentioned phonon-drag and electron-drag stress that is not temperature dependent. Figure 2.4.2 is a compilation of results relating to dislocation velocity and stress in many different metals (Meyers et al. 1984). As it can be seen, there are metals, like aluminium, copper, nickel, zinc and lithium, just to mention some of them, whose dislocations can be easily accelerated to very high velocity. It is clear that these metals must have a rather high strain rate sensitivity and that the dynamic effect shall prevail over the temperature one. We cannot conclude the discussion on strain rate effect on the
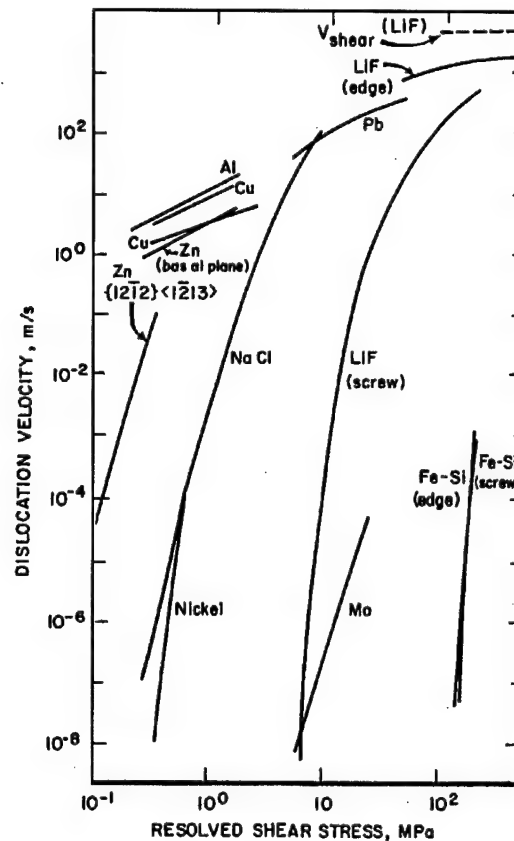

Figure 2.4.2 – Compilation of results in the literature relating dislocation velocities and stress (from M.A. Meyers and K.K. Chawla).

yield strength without mentioning twinning. It is now well recognized that in the competition between twinning and slip either an increase of strain rate or decreases of temperature favour twinning over slip dislocation motion. Normally, i.e., under quasi-static loading conditions, twinning occurs at very low temperatures. Meyers and Murr (1981) argued that this is a strong indication that twinning is not a thermally activated

23

mechanism. Indeed, measurements made by Takeuchi (1966) indicate that in iron twin propagates at 2,500 m/s and this velocity is virtually independent in the temperature interval – 196 °C t0 + 126 °C. Hence, the ratio τ/G, where G is the shear modulus, is not temperature dependent. This is schematically shown in Figure 2.4.3. At very low temperature the thermally activated dislocation motion becomes very difficult, no matter what the strain rate is. Twinning can prevail. Under quasi-static loading this condition is reached at very low temperature $T_{tw,qs}$. In carbon steels this can happen at – 200 °C. As the strain rate increases, the whole curve in Fig. 2.4.3 relative to conventional deformation by dislocation motion is translated up-wards so that the intersection of the two curves takes place at higher temperature T_{tw}: twinning becomes more probable. Finally, at extremely high strain rates slip by dislocation motion requires a stress higher than that needed to deform a crystal by twinning (curve c in Fig. 2.4.3). Under this limiting condition, twinning will always anticipate slip at any temperature and dislocation motion will be inhibited. We can assume, then, that the growth of yield strength by lowering the temperature or increasing the strain rate shall be limited to the value of the twinning stress. Therefore, it is reasonable to assume that this stress will represent the upper limit achievable at any temperature and strain rate; the upper athermal component of Figs. 2.2.7 and 2.2.8 is likely to be this twinning stress.
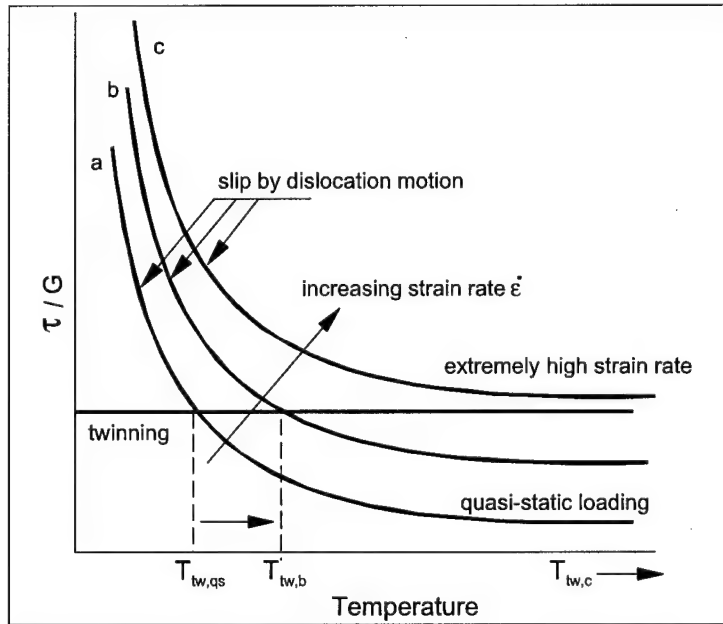

Figure 2.4.3 – Effect of strain rate on the temperature T_{tw} required to initiate twinning.

2.5. THE PRESENT RESEARCH

Figures 2.2.7 and 2.2.8 open the question of whether or not the plot should be left open. In other words, the straight lines representing the material trend appear to run without any end in the directions opposite to the merging points A and B. This seems not be physically acceptable, while it is rather convincing the opposite, i.e., that the material behavior diagram must have a closed form, which actually means that all the lines shall joint at both extremities, as shown in Figure 2.5.1. If this is the case, then a new formulation of the SSE can be written that takes the form:

$$\frac{\sigma_y - \sigma_o}{\sigma_{max} - \sigma_o} = 1 - \left[1 - \frac{ln(t / t_{min})}{ln(t_{max} / t_{min})}\right]^m \qquad (2.5.1)$$

where m is a strain rate exponent, σ_{max} the maximum value of the yield strength achievable at any strain rate at the minimum temperate T_{min}, σ_o the athermal component of the yield strength, $t = 1/T$, $t_{max} = 1/T_{min}$ and $t_{min} = 1/T_{max}$. For carbon steels T_{max} is the temperature at which the yield strength of the material starts to flatten afterward it drops abruptly, as schematically shown in Figure 2.5.2. The present research will address the
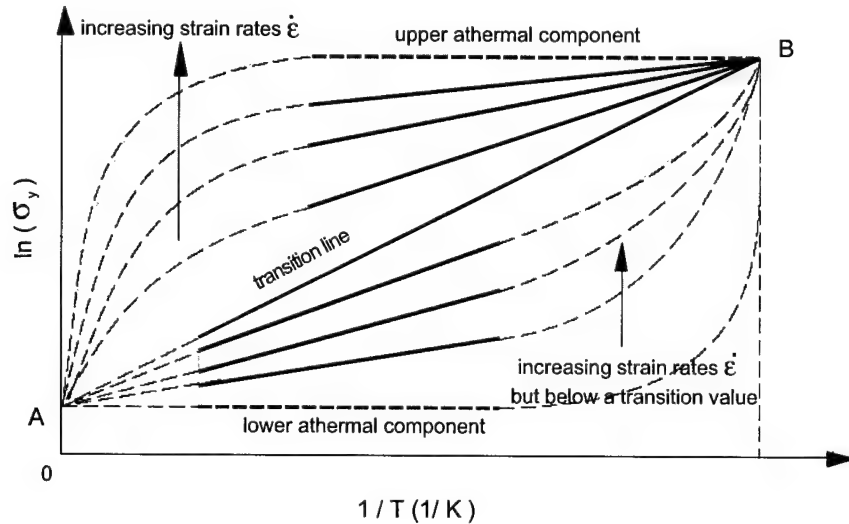

Figure 2.5.1 – Overall trend of the yield strength versus temperature at various strain rates. Eqs. 1 and 4 describe the linear trend shown in the figure by the strait solid lines.

issue of a unified solid state equation (USSE), represented by Eq. 2.5.1, that describes the dependence of the yield strength σ_y of any metal on temperature and strain rate, independently of its lattice structure, whether BCC or FCC or HPC. It will be shown how Eq. 2.5.1 is actually describing the behavior of metals like steels, niobium and α-titanium, already considered in the previous study, and OFHC copper. The domain of Eq. 2.5.1 is actually delimited by the values zero and one since both variables s_y and T have been normalized:

$$0 \leq \frac{t - t_{min}}{t_{max} - t_{min}} \leq 1$$

$$0 \leq \frac{\sigma_y - \sigma_o}{\sigma_{max} - \sigma_o} \leq 1 \tag{2.5.2}$$

where $t = 1/T$, σ_{max} is the maximum value of the yield strength achievable at any strain rate at the minimum temperate T_{min} (corresponding to the upper athermal component, point B in Figures 2.2.7 and 2.2.8), σ_o the lower athermal component of the yield strength (corresponding to point A in Figures 2.2.7 and 2.2.8), $t_{max} = 1/T_{min}$ and $t_{min} = 1/T_{max}$. For carbon steels, T_{max} is the temperature at which the trend of the yield strength σ_y seems to reach a constant value afterwards it drops abruptly, as schematically shown in Figure 2.5.2. The figure also gives a definition of the parameter T_{min}. In the competition between the deformation activated by dislocation motion and that caused by twinning, the former generally prevails, since it requires a lower stress. But this stress is temperature dependent and increases with decreasing temperature, as schematically shown in Figure 2.5.2. On the contrary, the twinning stress is temperature independent so that by decreasing the temperature a point is reached, T_{min}, where twinning will become the most probable mechanism of deformation, as described in the previous section. At this point the yield stress will not grow any longer, or will grow at a much lower rate, as schematically shown in Fig. 2.5.2 by line 1 and 2, respectively. Generally, in low alloy carbon steels dislocation motion is the dominant mechanism of deformation till about −200 °C. It is worth noting that below this minimum temperature, microscopic and even sub-microscopic cracks always present in a material can also
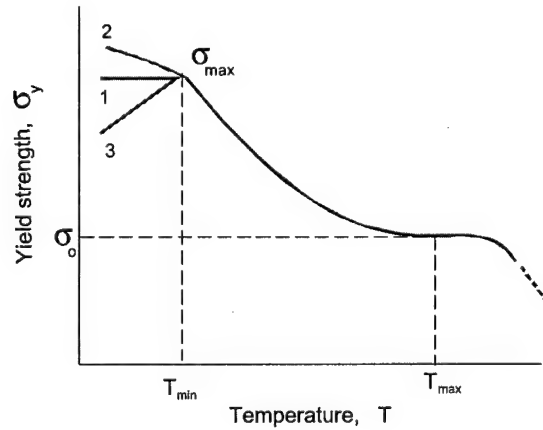

Figure 2.5.2 − Schematic of the yield strength σ_y versus temperature T in steels.

trigger a premature brittle fracture and this can explain the possible drop of the yield strength shown in Figure 2.5.2 by line 3. This latter behavior is normally seen on high strength steels. Of the five parameters that appear in Eq. 2.5.1, only four are really independent in that, as it will be shown, t_{max} is a function of t_{min}:

$$t_{max} = f(t_{min}) \tag{2.5.3}$$

26

Equation (5) can be re-written as:

$$1 - \frac{\sigma_y - \sigma_o}{\sigma_{max} - \sigma_o} = \left[1 - \frac{ln(t/t_{min})}{ln(t_{max}/t_{min})} \right]^m$$

$$\frac{\sigma_{max} - \sigma_y}{\sigma_{max} - \sigma_o} = \left[1 - \frac{ln(t/t_{min})}{ln(t_{max}/t_{min})} \right]^m \quad ;$$

$$ln\left(\frac{\sigma_{max} - \sigma_y}{\sigma_{max} - \sigma_o} \right) = m\left\{ ln\left[1 - \frac{ln(t/t_{min})}{ln(t_{max} - t_{min})} \right] \right\}$$

$$= m \cdot ln\left[ln\left(\frac{t_{max}}{t_{min}} \frac{t_{min}}{t} \right) \frac{1}{ln(t_{max}/t_{min})} \right] \qquad (2.5.4)$$

$$= m \cdot ln\, ln\left(\frac{t_{max}}{t} \right) - m \cdot ln\, ln\left(\frac{t_{max}}{t_{min}} \right)$$

Equation (2.5.4) describes a straight line in a *ln versus lnln* space whose slope is represented by the strain rate exponent m. The term $- m \cdot lnln(t_{max}/t_{min})$ is the known term, intersection of the straight line with the y axis, that we call M, then:

$$- m \cdot ln\, ln\left(\frac{t_{max}}{t_{min}} \right) = M$$

$$ln\left(\frac{t_{max}}{t_{min}} \right) = exp\left(-\frac{M}{m} \right) \qquad (2.5.5)$$

$$t_{max} = t_{min}\, exp\left[exp\left(-\frac{M}{m} \right) \right]$$

Equation (2.5.5) represents the cited relationship between t_{max} and t_{min}. Since both t_{max} and t_{min} are material constants it turns out that also the ratio $-M/m$ is a constant, defined positive, and is a characteristic of the material:

$$-\frac{M}{m} = Constant > 0 \qquad (2.5.6)$$

Equation (2.5.5) is plotted versus $-M/m$ in Figure 2.5.3, for several values of t_{min}. The plot can be of some help in deriving the values of the five constants that appear in Eq. (2.5.1), four of which are independent. In fact, knowing the value of t_{min} and t_{max} we can derive that of $-M/m$ or viceversa. It can be seen, from Figure 2.3.3, that for a carbon
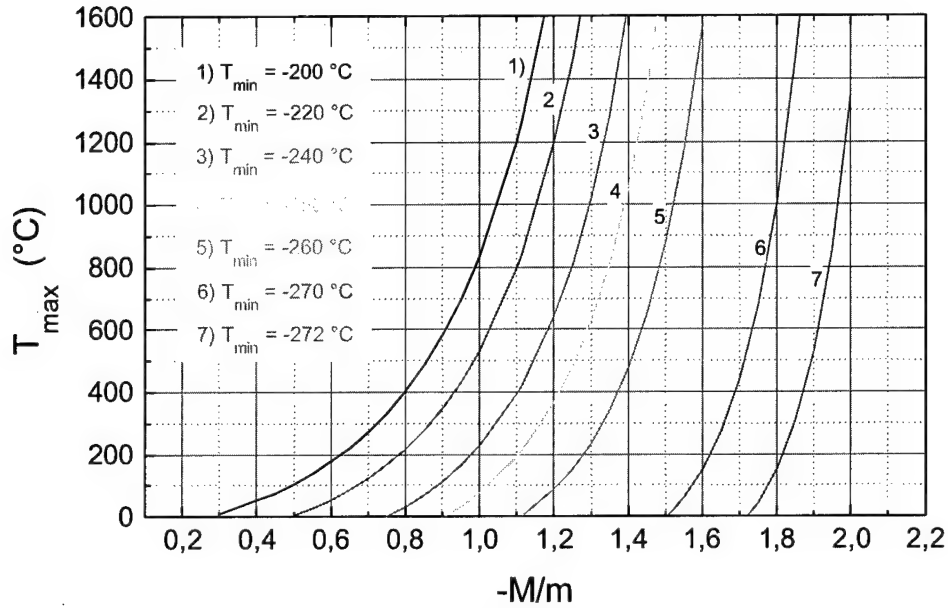
Figure 2.5.3 – Trend of eq. (2.5.5) for several selected values of T_{min}

steel of medium-low strength with $T_{max} \sim$ 500-600 °C and $T_{min} \sim$ -200 °C, the characteristic constant $-M/m$ shall have a value between 0.85 and 1.0. At variance, for a metal that doesn't show the typical trend of Fig. 2.5.2 and presents a T_{min} close to the absolute zero (line 6 or 7 of Fig.2.5.3), the ratio $-M/m$ shall range from 1.5 to more than two. Moreover, Eq. (2.5.4) describes a cluster of straight lines of the type:

$$y = ax - ab \qquad (2.5.7)$$

whose center C has co-ordinates $C \equiv (b;0)$. Therefore, all the straight lines described by Eq. (2.5.4) for the various strain rates, resulting in different m exponents, shall merge in a common center C of co-ordinates:

$$C \equiv \left(-\frac{M}{m}; \ 0 \right) \qquad (2.5.8)$$

This finding will be used, as it will be shown, as a check to verify the correct selection of the parameters σ_{max}, σ_o, t_{max} and t_{min} and infer the values of the strain rate exponents m.

28

3. ANALYSIS OF EXPERIMENTAL DATA

3.1. A 533 B STEEL

As first, we can start analyzing the behavior of a carbon steel already considered in the previous research, namely A 533 B. The SSE equation for this steel in the low strain rate domain and temperature range between 200 °C and – 175 °C was:

$$\sigma_y = 365\left(e^{120/T} \cdot \dot{\varepsilon}^{7.2/T}\right) \tag{3.1.1}$$

We know that Eq. (3.1.1) describes the dependence of the yield strength in the particular region of the low strain rates represented by the straight lines of Figure 2.5.1. We shall now derive the USSE for this steel valid in the full range of temperature and strain rates. The experimental results, already presented in the previous research are shown in Fig. 2.2.7. Let's start from Eq. 2.5.4 and re-plot the data of Fig. 2.2.7. We know that σ_y is about 2200 MPa while σ_o, the athermal component, is 365 MPa and $T_{min} \sim -200$ °C. Re-plotting the data according to Eq. (2.5.4) we obtain the graph of Figure 3.1.1. Effectively, all the trends of the experimental data are linear, as per Eq. (2.5.4) and converge towards the same point $C \equiv (0.84 \, ; \, 0)$. Therefore, the value of the constant $-M/m$ for A 533 B steel is:

$$-\frac{M}{m} = 0.84 \tag{3.1.2}$$

It is worth noting that Fig. 3.1.1 is based on the knowledge of $t_{max} = 1/T_{min}$. Once $-M/m$ is derived, Eq. (3.1.2), we can infer the value of $T_{max} = 1/t_{min}$ using Eq. (2.5.5) or the graphs of Fig. 2.5.3:

$$T_{max} \approx 500 \quad °C \tag{3.1.3}$$

The various slopes of the straight lines of Fig. 3.1.1 provide the values of the strain rate exponents m that will be used in Eq. (2.5.1). They are shown in TABLE 3.1.1 together with the M values and the corresponding strain rates $\dot{\varepsilon}$. Figure 3.1.2 presents the experimental results (open and closed points) obtained on A 533 B steel in a $(\sigma_y-\sigma_o)/(\sigma_{max}-\sigma_o) - (t-t_{min})/(t_{max}-t_{min})$ space and the corresponding predictions (solid lines) according to the proposed USSE, Eq. (2.5.1). Figure 2.16 shows the trend of the m exponent inferred from the slopes of the straight lines of Fig. 2.14 versus the natural logarithm of the corresponding stain rate $\dot{\varepsilon}$. The characteristic feature is that the data are aligned along two different lines that correspond to the two types of mechanisms that govern the plastic deformation in this alloy, namely the Peierls-Nabarro barrier and the viscous drag resistance. The two exponents, m_1 and m_2, have the following equations, respectively:

$$\begin{aligned} m_1 &= 0.154 + 0.019 \cdot \log\dot{\varepsilon} \\ m_2 &= 0.33 + 0.024 \cdot \log\dot{\varepsilon} \end{aligned} \tag{3.1.4}$$
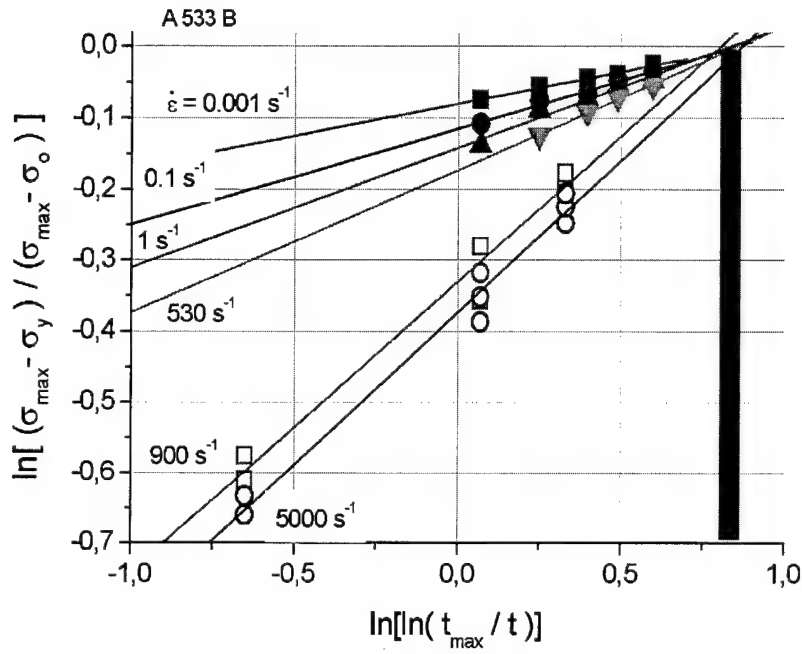
Figure 3.1.1 – Plot of A 533 B experimental data according to Eq. (2.5.4).

TABLE 3.1.1

Values of the strain rate exponent m at various strain rate for A 533 B steel

M	m	$\dot{\varepsilon}\ (s^{-1})$
−0.08	0.089	10^{-3}
−0.11	0.134	0.1
−0.14	0.169	1.0
−0.17	0.2	540
−0.33	0.41	900
−0.37	0.429	1600

In conclusion, the USSE for the A 533 B steel is:

$$\frac{\sigma_y - 365}{1835} = 1 - \left[1 - \frac{ln(740/T)}{2.32}\right]^m \qquad (3.1.5)$$

with the strain rate exponent given by Eq. (3.1.4) according to the strain rate domain in which the material is operating, low (below 1000 s^{-1}) or high (above 1000 s^{-1}).
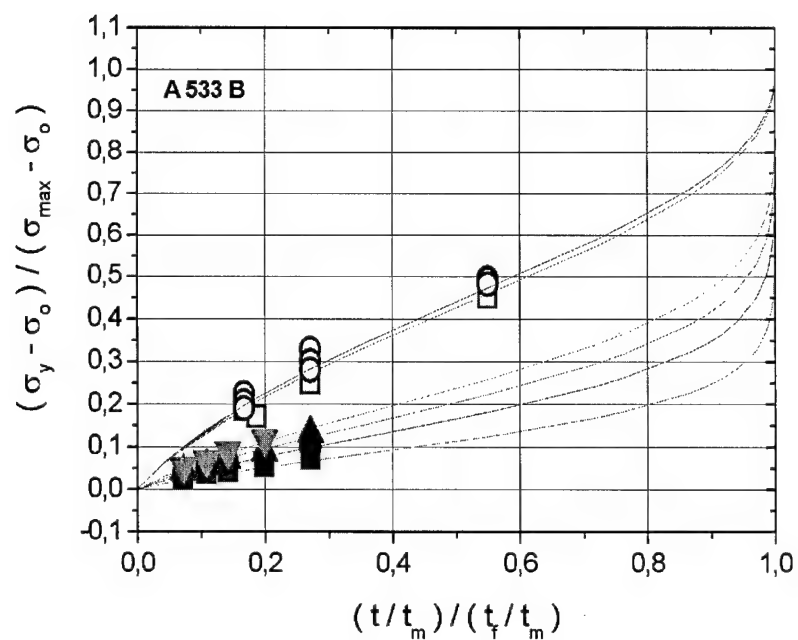
Figure 3.1.2 – Experimental data (open and closed symbols) and USSE predictions (solid lines) according to Eq. (2.5.1) for A 533 B steel.
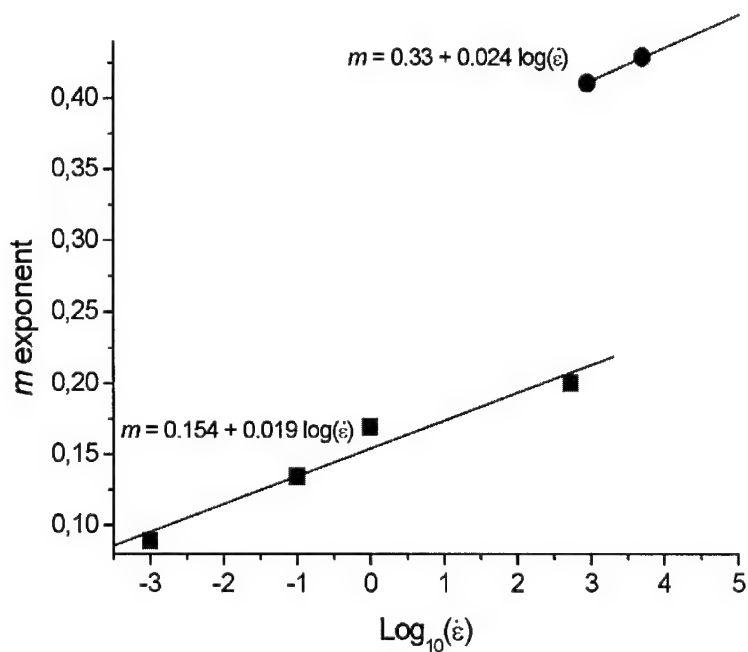

Figure 3.1.3 – Trend of the m exponent vs the log($\dot{\varepsilon}$) for A 533 B steel.

3.2. A 537 STEEL

The second analysis focuses on the A 537 steel already considered in the previous research. For this steel the constitutive equation found was:

$$\sigma_y = 245 \cdot \left(e^{153/T} \cdot \dot{\varepsilon}^{8.3/T} \right) \tag{3.2.1}$$

As previously said, Eq. (3.2.1) is actually representing the behavior of the material in the limited domain represented by the straight lines of the bottom part of Fig. 2.2.7. We shall now reanalyze the experimental data according to Eq. (2.5.1) that, on the contrary, is describing the entire evolution of the yield strength for any temperature and strain rate. As first, as already done for A 533 B steel, let's analyze the data according to Eq. (2.5.4). The results are shown in Figure 3.2.1. Again, the data are well aligned along straight lines, as predicted by Eq. (2.5.4), and merge in a common point C whose co-ordinates provides the value of the constant $-M/m$. The intersections with the y axis (M), the slopes and the relative strain rates are reported in TABLE 3.2.1 Finally, Figure 3.2.2 presents the experimental results (closed and open points) and the theoretical prediction of Eq. (2.5.1) (solid lines).
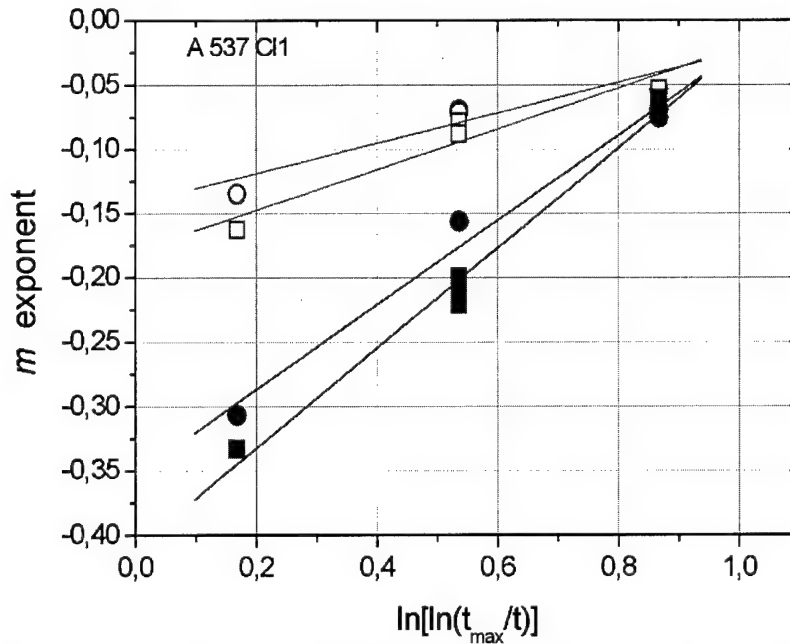

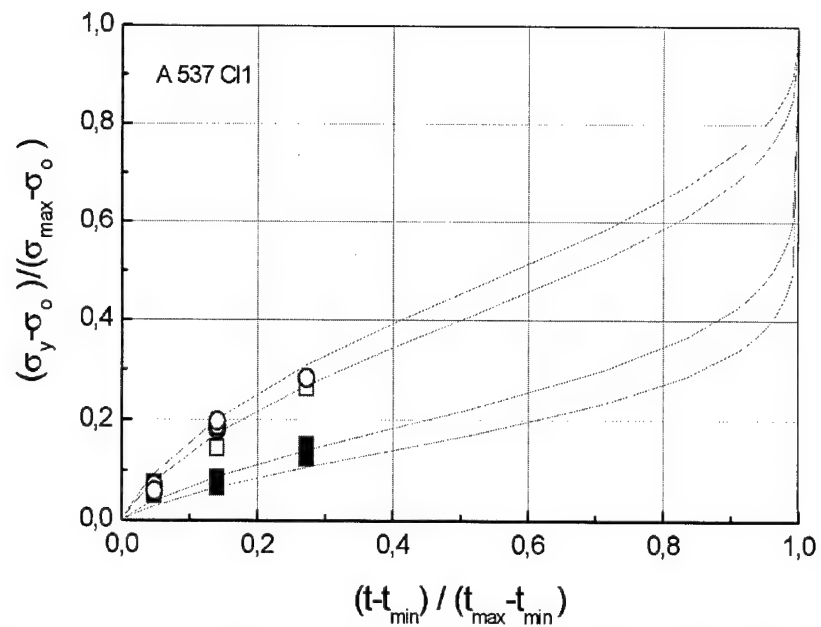*Figure 3.2.1 – Plot of A 537 Cl1 experimental data according to Eq. (2.5.4).*

Figure 3.2.2 – Experimental data (closed and open symbols) and USSE predictions (solid lines) according to Eq. (2.5.1) for A 537 Cl1 steel.

TABLE 3.2.1

Values of the strain rate exponent m at various strain rate for A 537 Cl1 steel

M	m	$\dot{\varepsilon}\ (s^{-1})$
-0.142	0.12	10^{-3}
-0.179	0.158	1.0
-0.353	0.329	400
-0.41	0.389	1300

3.3. A 508 CL3 STEEL

The third analysis deals with the A 508 Cl3 steel already considered in the previous research. The experimental data of Fig. 2.2.8 are re-plotted according to the procedures outlined in the previous paragraphs yielding the results shown in Figure 3.3.1 and Figure 3.3.2. The intersections M with the y-axis of Fig. 3.3.1, slopes m and the relative strain rates are reported in TABLE 3.3.1.
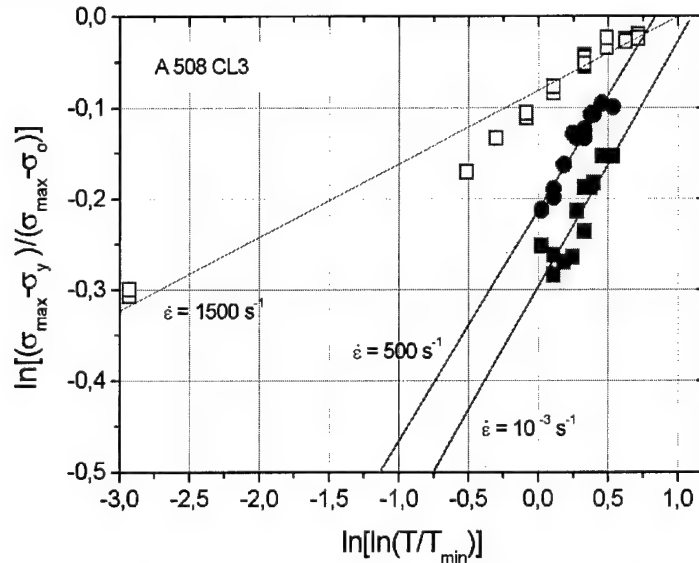

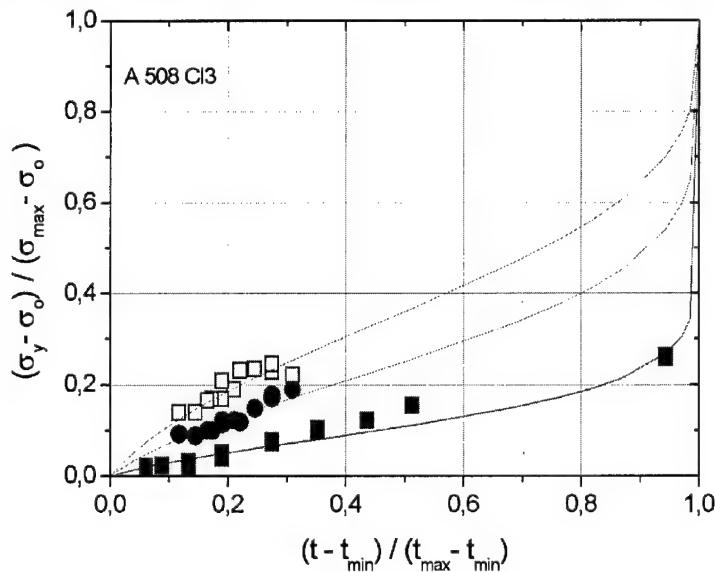*Figure 3.3.1 – Plot of A 508 Cl3 experimental data according to Eq. (2.5.4).*

Figure 3.3.2 – Experimental data (closed and open symbols) and USSE predictions (solid lines) according to Eq. (2.5.1) for A 508 Cl3 steel.

34

TABLE 3.3.1

Values of the strain rate exponent m, of the intersection M and the constant −M/m at various strain rate for A 508 Cl3 steel

−M/m	M	m	$\dot{\varepsilon}$ (s-1)
0.987	-0.079	0.08	10-3
0.82	-0.211	0.257	500
1.05	-0.295	0.271	1500

3.4. NIOBIUM

Niobium represents a study case particularly interesting. It is not a ferritic steel, but it has the same BCC lattice that makes this metal sensitive to both temperature and strain rate. Its melting temperature is about 2.500 °C. Its constitutive equation found in the previous research, representing the behavior of the material in the limited domain delimited by the straight lines of the bottom part of Fig. 2.5.1 is:

$$\sigma_y = 90 \cdot \left(e^{689/T} \cdot \dot{\varepsilon}^{39/T} \right) \tag{3.4.1}$$

The athermal component of the yield strength of this metal, that is very sensitive to the strain rate $\dot{\varepsilon}$ (very high value of the exponent ~39), is equal to 90 MPa. This dependency of the yield strength on $\dot{\varepsilon}$ is so marked that a strain rate of only 0.48 s^{-1} is already high enough to bring the material in the upper part of the diagram of Fig. 2.5.1, while in carbon steels this happens only above 500-600 s^{-1}. The strain rates analyzed for this metal ranged from 0.00016 to 63 s^{-1}. A strain rate of only 0.48 s^{-1} makes the metal respond with yield strength of about 813 MPa already at room temperature (RT). Just for comparison, carbon steel like A 533 B at RT has yield strength of only 535 MPa under the same strain rate of 0.48 s^{-1}. Figure 3.4.1 shows the experimental data for niobium analyzed according to Eq. (2.5.4). TABLE 3.4.1 lists the results obtained from the analysis.

TABLE 3.4.1

Values of the strain rate exponent m of the intersection M with the y axis and the constant −M/m for niobium at various strain rate.

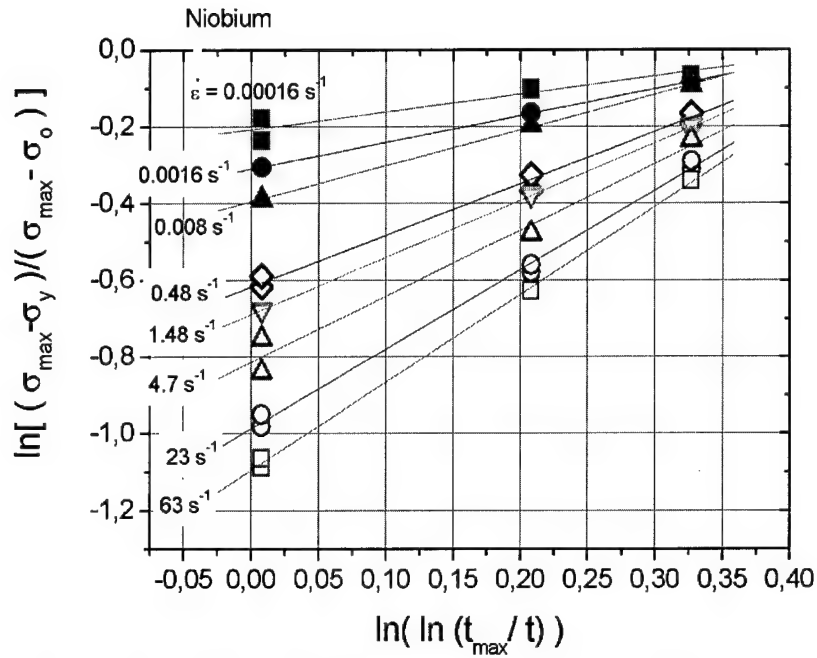| −M/m	M	m	$\dot{\varepsilon}$ (s^{-1})
0.435	-0.2	0.46	0.00016
0.443	−0.31	0.7	0.0016
0.42	−0.39	0.93	0.008
0.459	−0.62	1.35	0.48
0.463	−0.69	1.49	1.48
0.47	−0.81	1.72	4.7
0.47	−0.99	2.1	23
0.478	-1.1	2.3	63

Figure 3.4.1 – Plot of niobium experimental data according to Eq. (2.5.4).
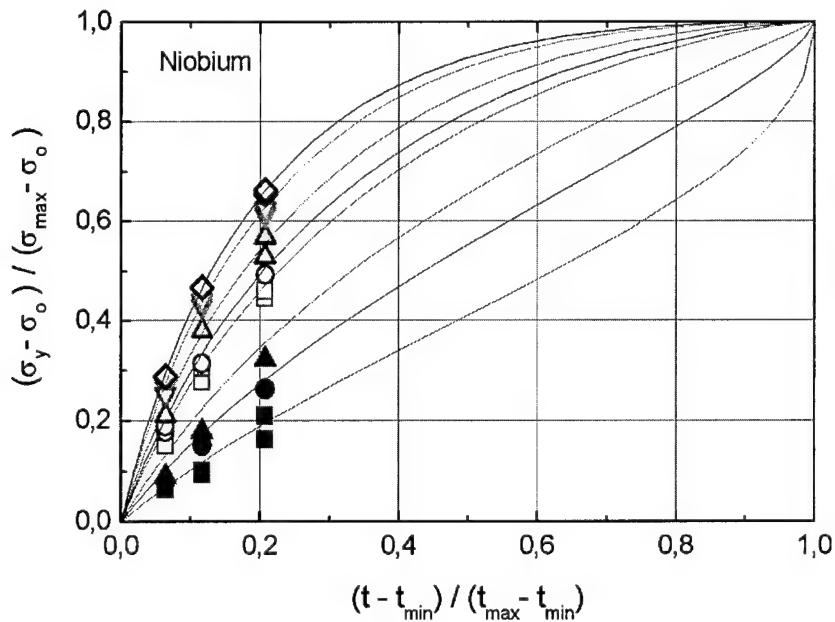

Figure 3.4.2 – Experimental data (closed and open symbols) and USSE predictions (solid lines) according to Eq. (2.5.1) for niobium.

The trends are linear, as predicted by Eq. (2.5.4) and converge towards the same common point C of co-ordinates $C \equiv (-M/m \; ; \; 0)$ The same data plotted according to Eq. (2.5.1) are presented in Fig. 3.4.2. The values of the four constants σ_o, σ_{max}, T_{max} and T_{min} are the followings:

$$\sigma_o \;=\; 90 \;\; MPa; \;\; \sigma_{max} \;=\; 1000 \;\; MPa; \;\; T_{max} \;=\; 100 \;\; °C; \;\; T_{mim} \;=\; -200 \;\; °C$$

Of great interest is the trend of the strain rate exponent m with $\dot{\varepsilon}$, shown in Figure 1.23. The characteristic feature is that the strain rate exponents m appear to be aligned along a straight line of equation:

$$m \;=\; 1.58 + 0.32 \cdot log_{10}(\dot{\varepsilon}) \tag{3.4.2}$$

Therefore, the USSE for niobium is:

$$\frac{\sigma_y - 90}{900} \;=\; 1 - \left[1 - \left(\frac{ln(373/T)}{1.6} \right) \right]^m \tag{3.4.3}$$

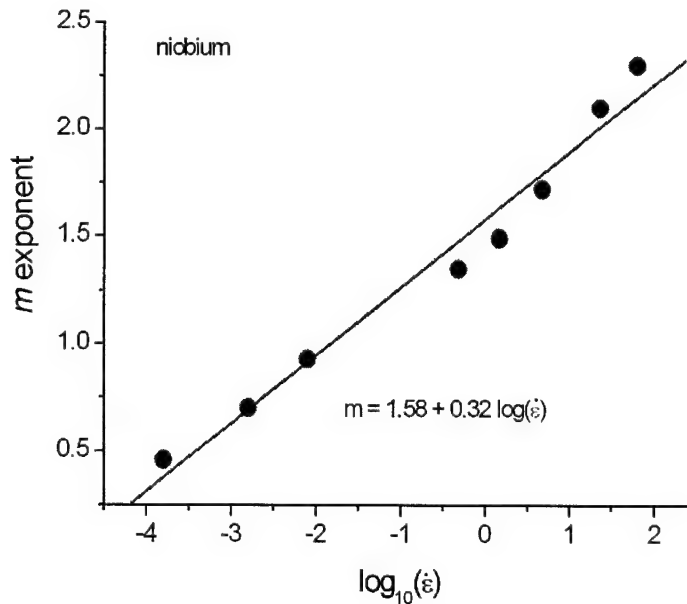with the exponent m given by Eq. (3.4.2).

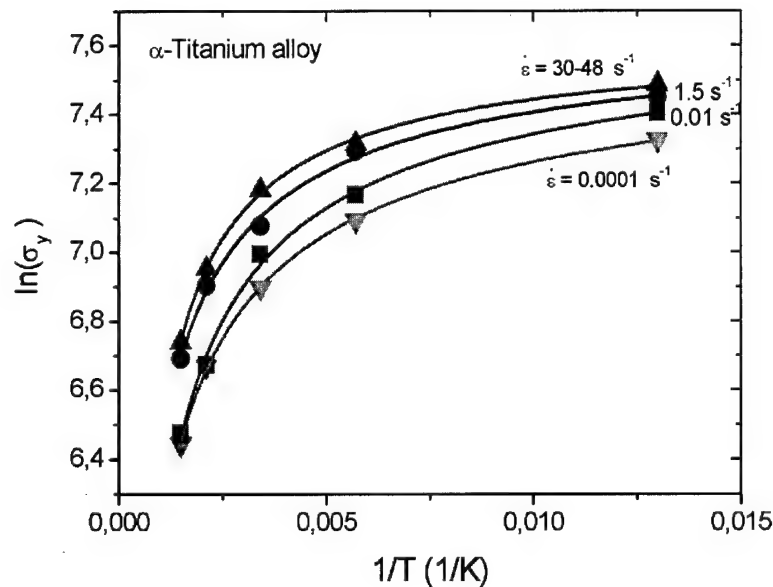Figure 3.4.2 – Trend of the strain rate exponent m versus log($\dot{\varepsilon}$) for niobium.

3.5. α-TITANIUM ALLOY.

Let's now analyze a α-titanium alloy. This metal has a HCP lattice. Because of that the yield strength is not presenting the characteristic linear trend versus $1/T$ in a semi-log scale, shown by BCC metals. This can be seen in Figure 3.5.1. The reanalysis of the experimental data according to Eq. (2.5.4) yields the diagram of Figure 3.5.2. In spite of the different structure, the data points seem to follow the linear trend predicted by Eq. (2.5.1) and merge in a common point C of co-ordinates $C \equiv (-M/m ; 0)$. TABLE 3.5.1 summarizes the slopes m, the intersections M and the ratios $-M/m$ at the various strain rates considered in the testing program.

TABLE 3.5.1
Values of the strain rate exponent m, intersection M with the y axis and ratios –M/m at for various strain rate in α-titanium alloy.

–M/m	M	m	$\dot{\varepsilon}\ (s^{-1})$
1.6	−2.05	1.276	0.001
1.55	−2.52	1.627	0.01
1.61	−2.87	1.78	1.5
1.596	−3.24	2.03	35

Figure 3.5.1 – Trend of experimental yield strengths (solid points) vs 1/T at various strain rates for α-titanium alloy.

The analysis of the same data is presented in Figure 3.5.3 (solid points) together with the theoretical prediction according to Eq. (2.5.1) (solid lines) for the various strain rates considered. The values of the four constants σ_o, σ_{max}, T_{max} and T_{min} are the followings:

$$\sigma_o = 100 \quad MPa; \quad \sigma_{max} = 2000 \quad MPa; \quad T_{max} = 1650 \quad °C; \quad T_{mim} = -260 \quad °C$$

Therefore, the USSE for α-titanium alloy is:

$$\frac{\sigma_y - 100}{1900} = 1 - \left[1 - \left(\frac{ln(1923/T)}{5} \right) \right]^m \tag{3.5.1}$$

with the value of the m exponent given by Eq. (3.5.2). A detail of Fig. 3.5.2, for a restricted field of $(t-t_{min})/(t_{max}-t_{min})$ ranging between zero and 0.25, is presented in Figure 3.5.3. The trend of the m exponents with the $log_{10}(\dot{\varepsilon})$ is reported in Figure 3.5.4. The equation of the best-fit line is:

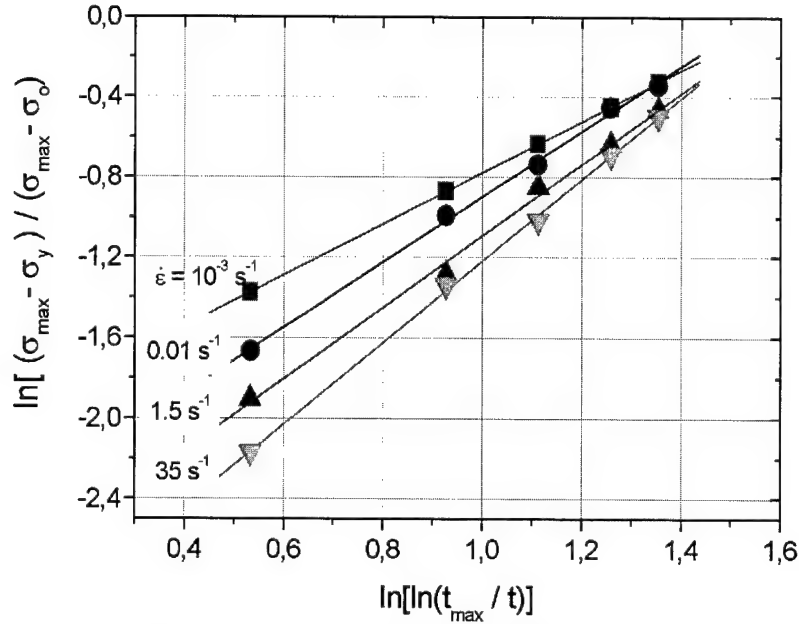$$m = 1.8 + 0.15 \cdot log_{10}(\dot{\varepsilon}) \tag{3.5.2}$$

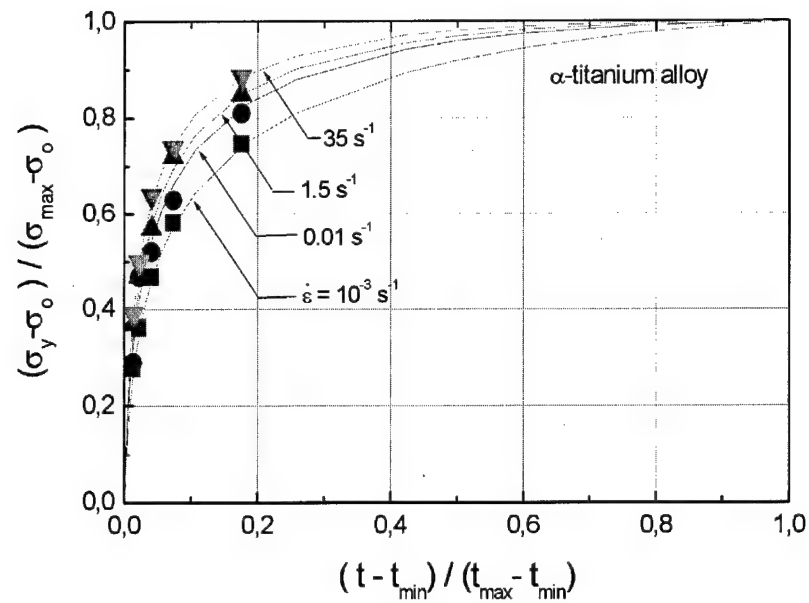Figure 3.5.2 – Trend of experimental data according to Eq. (2.5.4) for α-titanium alloy.

Figure 3.5.3 – Trend of experimental data (solid points) and theoretical predictions (solid lines) according to Eq. (2.5.1) for α-titanium alloy.
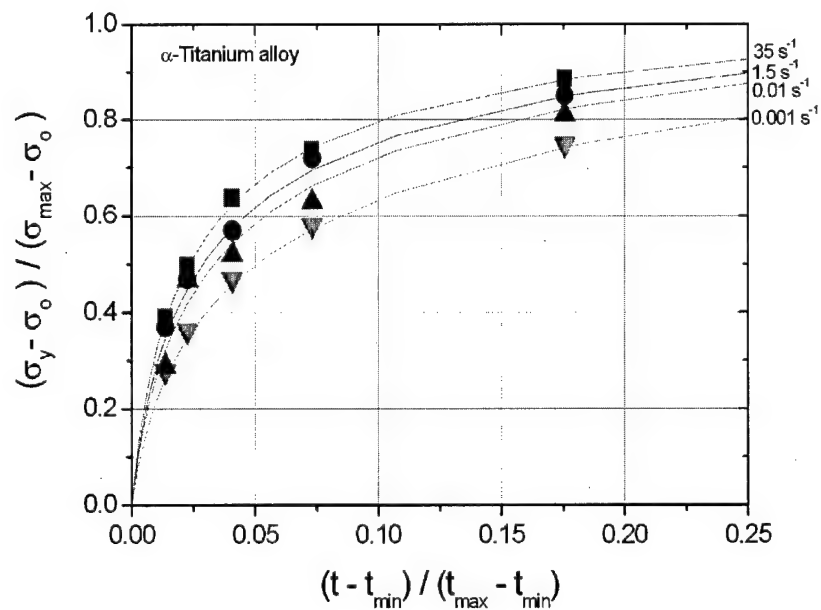

Figure 3.5.4 – Detail of experimental data (solid points) and theoretical predictions (solid lines) of Figure 3.5.3 for α-titanium alloy.
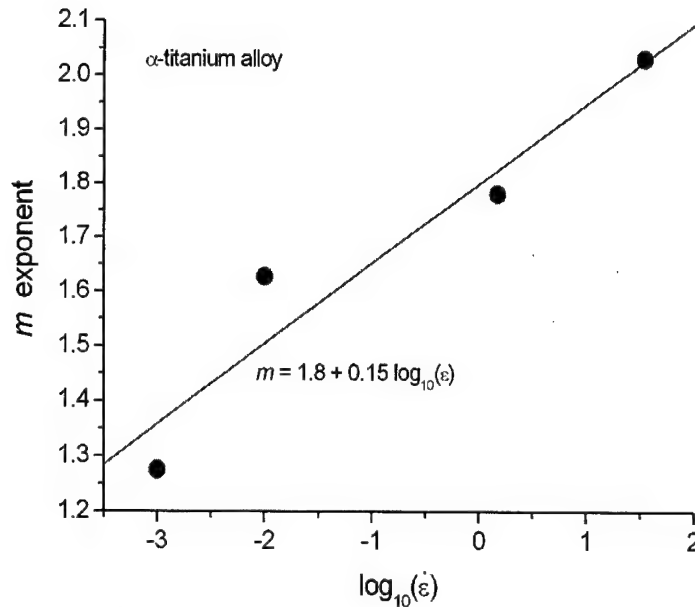
Figure 2.28 – Trend of the strain rate exponent m for α-titanium.

3.6. OFHC COPPER

The last metal considered in this study is OFHC Copper. Specimen were prepared from a 10 mm thick plate and given a 600 °C annealing heat treatment in argon followed by slow quenching. The yield values at strain rates of 10^{-4}, 0.1, 10 and 1000 s^{-1}, respectively, are shown in Figure 3.6.1. The same data, plotted in the usual ln vs $1/T$ diagram, are presented in Figure 3.6.2. The linear trend, typical of BCC steel is lost, as already seen for a-titanium alloy. Yet, the convergence of all data towards a common upper and lower value is maintained. Let's start analyzing the data according to Eq. (2.5.4). OFHC copper is a typical metal having a T_{min} close to the absolute zero. Accordingly, the graph of Fig. 2.5.3 anticipates a $-M/m$ value over 1.7-1.8. In fact, plotting the data in a $ln[(s_{max}-s_y)/(s_{max}-s_o)]$ versus $lnln(T/T_{min})$ according to Eq. (2.5.4), we get the graph of Figure 3.6.3. As predicted by the proposed USSE, in this space the trends are linear and all lines converge in the same point whose abscissa provides the value of the ratio $-M/m$ that, in this particular case, is equal to 2.32, i.e., larger than 1.7-1.8 as expected. TABLE 3.6.1 lists the values of M, m and the corresponding ratio $-M/m$ at each strain rate considered.
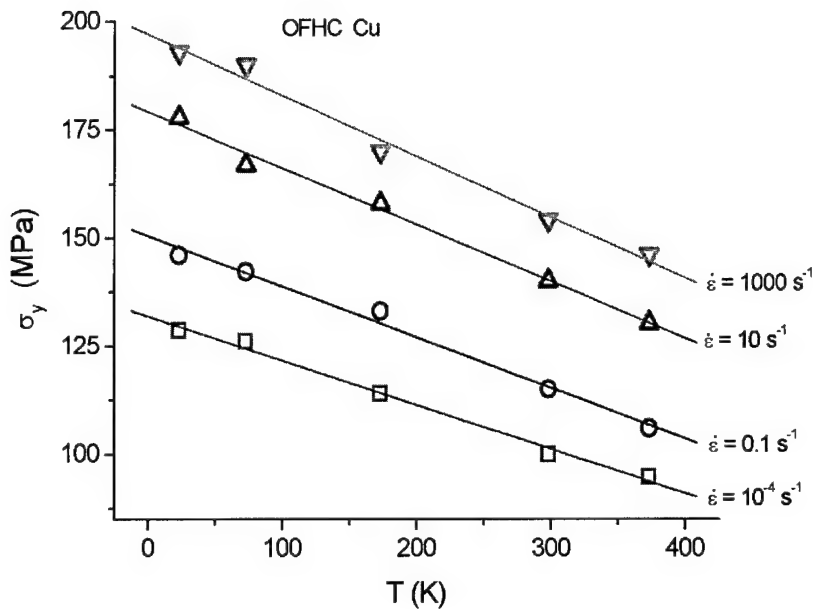
41

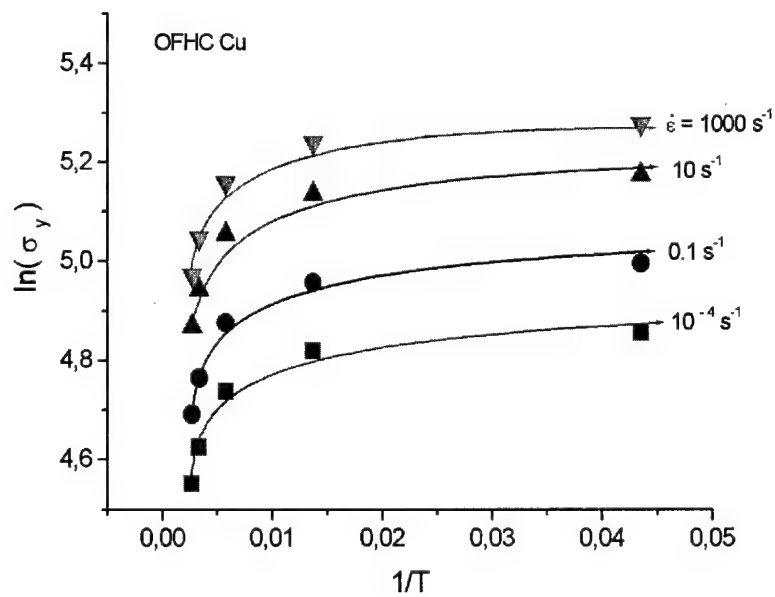*Figure 3.6.1 – Trend of the yield strength versus temperature for OFHC Copper.*

Figure 3.6.2 – Trend of ln(σ_y) vs 1/T observed on OFHC Copper at various strain rates.

TABLE 3.6.1

Values of the intersection M, the strain rate exponent m and their ratio for the strain rates considered in this analysis.

$-M/m$	M	m	$\dot{\varepsilon}$ (s^{-1})
2.2	−5.37	2.43	10^{-4}
2.35	−7.8	3.31	0.1
2.38	−9.83	4.13	10
2.34	−14.99	6.4	1000

It can be seen that the ratio $-M/m$ is practically constant, as it should be. The same data reanalyzed according to the Eq. (2.5.1) yield the plot of Figure 3.6.4. The collocation of data over the entire scale, from 0 to 1, is finally presented in Figure 3.6.5.
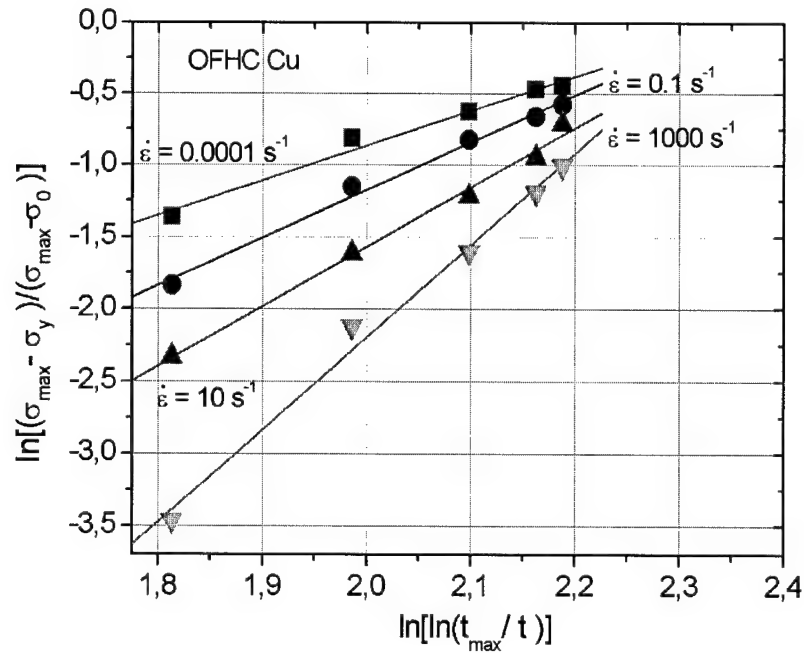

Figure 3.6.3 – Trend of experimental data according to Eq. (2.5.4) for OFHC copper.
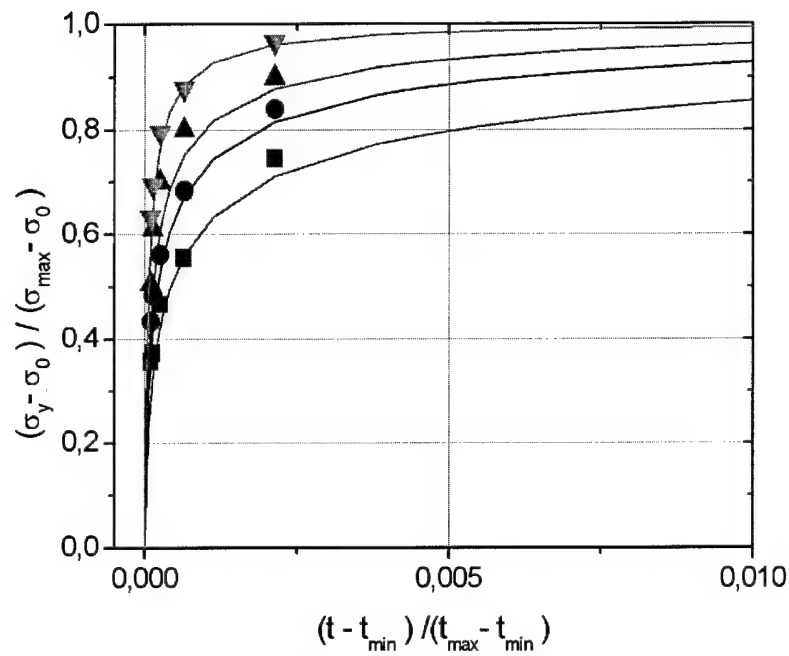
Figure 3.6.4 – Detail of data (solid points) and theoretical predictions (solid lines) according to Eq. (2.5.1) for OFHC copper.
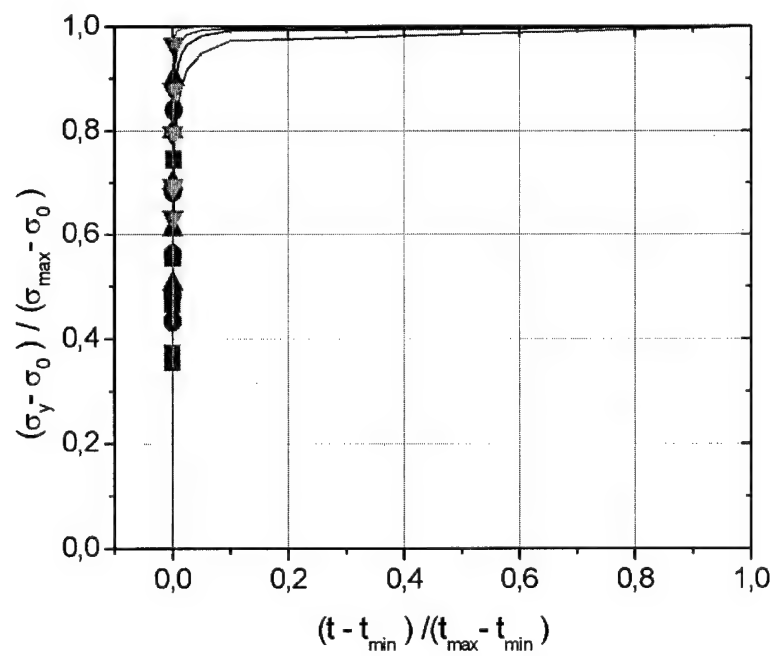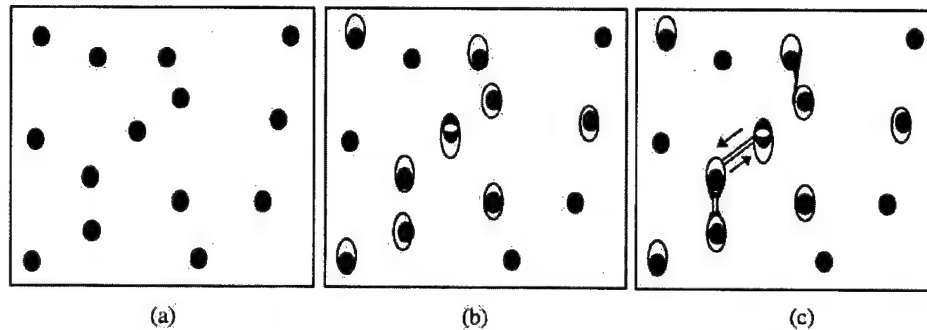

Figure 3.6.5 – Trend of data (solid points) and theoretical predictions (solid lines) according to Eq. (2.5.1) for OFHC copper.

4. DUCTILE DAMAGE MODEL BACKGROUND

In the last decades it has been shown that local approaches have a great potential in predicting the occurrence of failure in specimens, components and structures. Today it is well assessed that ductile failure occurs as a result of microvoids nucleation and growth at inclusions, as sketched in Figure 4.1 and Figure 4.2

(a)   (b)   (c)

Figure 4.1 – Ductile failure micromechanism: a) distribution of hard included particles, b) void nucleation at deformation threshold stage due to particle-matrix debonding, c) growth and coalescence prior final rupture

Figure 4.2 - Void growth and coalescence in copper

The local approach to fracture is based on the assumption that, if the microscopic mechanism of failure is known, the modification of the material constitutive response can be predicted from micromechanical considerations. Consequently, direct transferability from material to structure, without any geometry effect, would be one of the key features.

Many theoretical models have been proposed in the literature that can be grouped in two main sets: continuum damage mechanics (CDM) based models and porosity models.

Porosity models, derived from the Gurson type model, are based on the modification of the yield function as a result of the increasing porosity with plastic strain, Gurson

(1977). Here, porosity plays the role of a softening variable that progressively implodes the yield surface in order to account for damage effects.

CDM models are developed in the framework of continuum mechanics. Here, damage effects are accounted by a thermodynamic variable, D, that reduces material stiffness. Thus, the complete set of constitutive equations for the material undergoing damage is derived.

Both approaches suffer major limitations. Porosity models usually require a large number of material parameters, none of which has a physical meaning, that have to be identified using coupled numerical simulation and experiments. On the other side, CDM model performance depends on the assumed form for the dissipation potential from which damage evolution law can be derived by normality rule. All the models proposed in the literature show material dependency, lack of performance under multi-axial state of stress conditions and temperature and strain rate effect is usually neglected.

In 1997 Bonora proposed a new non-linear CDM model for ductile failure that overcome material dependency and stress triaxiality effects. The model resulted successful in predicting notched and cracked components response using only information, such as damage parameters, identified in simple uniaxial state of stress condition, (Bonora, 1998). An example of this is given in Figure 4.3 and Figure 4.4 where the applied load versus necking diameter reduction response, in standard uniaxial tension test, has been used to identify damage parameters used, successively, to predict material crack resistance curve.
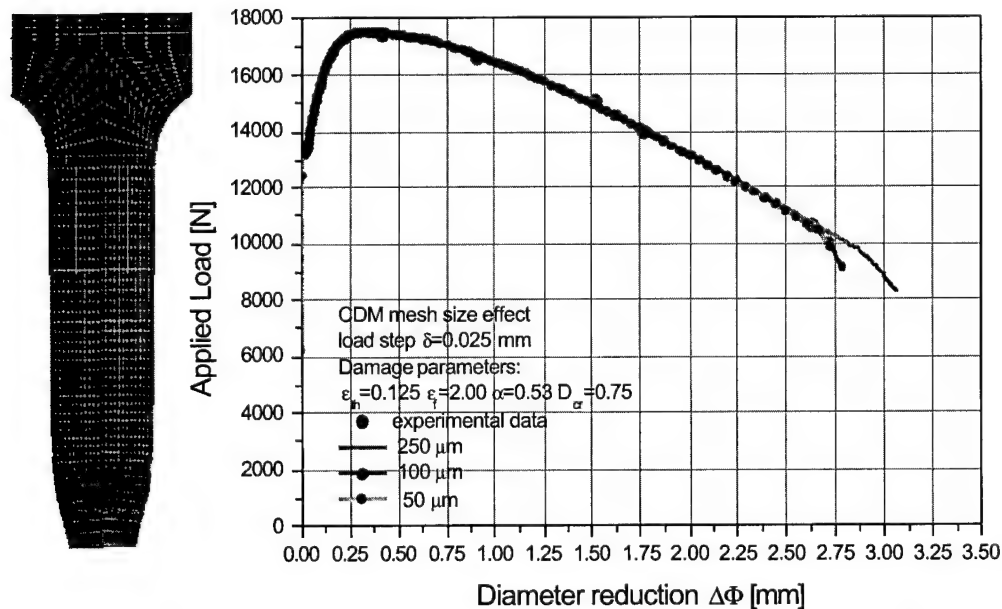

Figure 4.3 – 22NiMoCr37 steel tensile response simulation using damage model: each curve has been obtained for different mesh size at the fracture location. On the left, mesh shows neck profile and damage contours at fracture
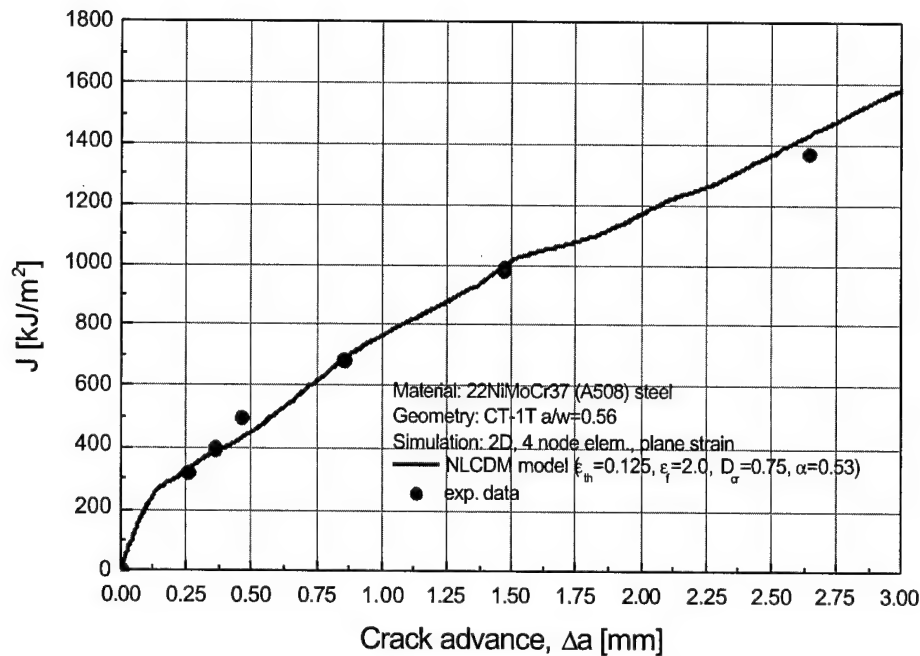
Figure 4.4 – Predicted crack resistance curve for 22NiMoCr37 and comparison with experimental data

Later, Bonora and Milella (2001) extended the damage model in order to incorporate temperature and strain rate effects.

Up to now, very little attention have been given to the mechanics of ductile deformation and damage under compressive state of stresses. This issue becomes very important in order to understand and predict component life under low cycle fatigue regime or under intense dynamic loading in which damage accumulation is related to the bouncing motion of strain waves into the body.

Bonora and Newaz (1998) demonstrated the possibility to predict low cycle fatigue life at ductile crack growth initiation discussing possible integration scheme for the non-linear damage law. At the moment, as far as the authors are aware of, no attempt to extend CDM model formulation to cyclic loading under variable stress triaxiality loading conditions has been made. In the following sections, for the first time, the non-linear damage model proposed by Bonora has been extended to negative stress triaxiality loading condition, based on simple physical considerations, introducing a new internal variable associated to damage D.

The model, implemented in form of user subroutine in the finite element code MSC/MARC, has been tested on single FEM element under simple loading conditions such a as normal and shear stress. At the present time, the model is going to be use in the research contract SPC F61775-01-C-0003 supported by AFOSR for an extensive study on impact damage and penetration mechanics of ductile targets.

47

5. NON-LINEAR CDM MODEL FOR DUCTILE FAILURE

Lemaitre (1985) firstly defined the CDM framework for plasticity damage. Damage accounts for material progressive loss of load carrying capability due to irreversible microstructural modifications, such as microvoids formation and growth, microcracking, etc. From a physical point of view, damage can be expressed as

$$D_{(n)} = 1 - \frac{A_{eff}^{(n)}}{A_0^{(n)}} \tag{5.1}$$

where, for a given normal n, $A_0^{(n)}$ is the nominal section area of the RVE and $A_{eff}^{(n)}$ is the effective resisting one reduced by the presence of micro-flaws and their mutual interactions.

Even though this definition implies a damage tensor formulation, the assumption of isotropic damage leads to a more effective description where the scalar D can be simply experimentally identified. Additionally, this assumption is not too far from reality as a result of the random shapes and distribution of the included particles and precipitates that trigger plasticity damage initiation and growth. The strain equivalence hypothesis gives the operative definition of damage as:

$$D = 1 - \frac{E_{eff}}{E_0} \tag{5.2}$$

where E_0 and E_{eff} are the Young's modulus of the undamaged and damaged material, respectively.

The complete set of constitutive equation for the damage material can be derived assuming that:

- a damage dissipation potential f_D, similarly to the one used in plasticity theory, exists;

- no coupling between damage and plasticity dissipation potentials exists;

- damage variable, D, is coupled with plastic strain;

- the same set of constitutive equations for the virgin material can be used to describe the damaged material replacing only the stresses with the effective ones and assigning a state equation for D.

Bonora (1997) proposed the following expression for the damage dissipation potential,

$$f_D = \left[\frac{1}{2} \left(-\frac{Y}{S_0} \right)^2 \cdot \frac{S_0}{1-D} \right] \cdot \frac{(D_{cr} - D)^{\frac{\alpha-1}{\alpha}}}{p^{\frac{2+n}{n}}} \tag{5.3}$$

where, D_{cr} is the critical value of the damage variable for which ductile failure occurs, S_0 is a material constant and n is the material hardening exponent. α is the damage

exponent that determines the shape of the damage evolution curve and is related to the nature of the bound between brittle inclusions and the ductile matrix. Thus, the constitutive equation set for isotropic hardening material is given by:

strain decomposition

$$\dot{\varepsilon}_{ij}^{T} = \dot{\varepsilon}_{ij}^{e} + \dot{\varepsilon}_{ij}^{p} \tag{5.4}$$

elastic strain rate

$$\dot{\varepsilon}_{ij}^{e} = \frac{1+v}{E} \frac{\dot{\sigma}_{ij}}{1-D} - \frac{v}{E} \frac{\dot{\sigma}_{kk}}{1-D} \delta_{ij} \tag{5.5}$$

plastic strain rate

$$\dot{\varepsilon}_{ij}^{p} = \dot{\lambda} \frac{\partial f_{p}}{\partial \sigma_{ij}} = \dot{\lambda} \frac{3}{2} \frac{\dot{s}_{ij}}{1-D} \frac{1}{\sigma_{eq}} \tag{5.6}$$

plastic multiplier

$$\dot{r} = -\dot{\lambda} \frac{\partial f_{p}}{\partial R} = \dot{\lambda} = \dot{p}(1-D) \tag{5.7}$$

kinetic law of damage evolution

$$\dot{D} = -\dot{\lambda} \frac{\partial f_{D}}{\partial Y} = \alpha \cdot \frac{(D_{cr} - D_{0})^{\frac{1}{\alpha}}}{\ln(\varepsilon_{f}/\varepsilon_{th})} \cdot f\left(\frac{\sigma_{H}}{\sigma_{eq}}\right) \cdot (D_{cr} - D)^{\frac{\alpha-1}{\alpha}} \cdot \frac{\dot{p}}{p} \tag{5.8}$$

Detailed description on the derivation of these Equations can be found elsewhere, (Bonora, 1997). In Equation (9) stress triaxiality effects are accounted by the function $f(\sigma_H/\sigma_{eq})$ defined as,

$$f\left(\frac{\sigma_{H}}{\sigma_{eq}}\right) = \frac{2}{3}(1+v) + 3 \cdot (1-2v) \cdot \left(\frac{\sigma_{H}}{\sigma_{eq}}\right)^{2} \tag{5.9}$$

that is derived assuming that ductile damage mechanism is governed by the total elastic strain energy, Lemaitre (1985). Here, $\sigma_H = \sigma_{kk}/3$ is the hydrostatic part of the stress tensor and v is the Poisson's ratio. The model requires five material parameters in order to be applied.

The strain threshold (in uniaxial monotonic loading) ε_{th}, at which damage processes are activated; the theoretical failure strain ε_f, at which ductile failure under completely uniaxial state of stress conditions occurs; the initial amount of damage present in the material, D_0; the critical damage, D_{cr}, at which failure occurs and the damage exponent, α, that control the shape of damage evolution with plastic strain. Experimental procedure for damage parameters identification can be found elsewhere, (Bonora, 1999).

6. DAMAGE MODEL: EXTENSION TO HIGH STRAIN RATE

CDM damage model, and porosity based damage models as well, do not incorporate effect related to strain rates or temperature. Ping (1994) theoretically analyzed the modification resulting from dynamic loading onto the growth rate of cavities in a ductile matrix including inertial effect, but without the support of experimental evidences.

The possibility to obtain direct damage measurements under high strain rates, according to the procedure indicated by Bonora (1999), is very limited. It would require high strain velocity controlled test and adequate strain gauge instrumentation capable to resist to repeated high velocity deformation process.

Bonora and Milella (2000) performed damage measurement in the low strain rate range (<0.1 s^{-1}) observing no effect on damage evolution law. At the same time, experimental observations confirm that the formation and growth of microcavities, no matter what both the temperature and the strain rate are, always control ductile failure mechanism. Consequently, Bonora and Milella postulated that the damage potential should remain unchanged and should not depended explicitly on strain rate and temperature. On the contrary, damage parameters, that represent material specific physical quantities, should show some variability in association with them.
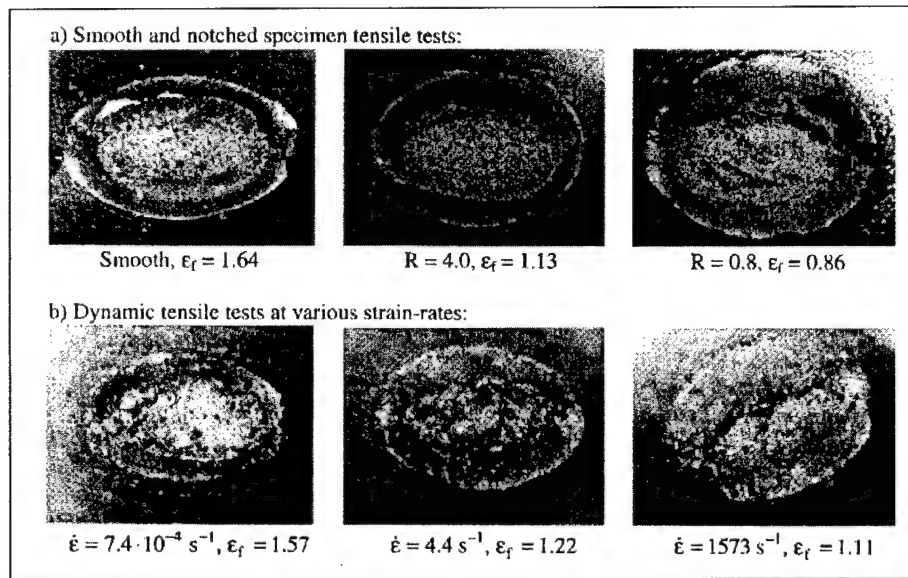

Figure 6.1 – Strain rate, ε_f and diameter at fracture in smooth and notched tensile bar in steel, (Bowik et al., 1999)

Due to the impossibility to deal with direct damage measurement at high strain rates, it is possible to obtain some important information comparing measures relative to two of four of material damage parameters, i.e. ε_{th} and ε_f, obtained under high strain rate. Johnson *et al.* (1983) investigated the behavior of several classes of metals under severe load rates and temperature. They analyzed the dependence of strain to failure with $\dot{\varepsilon}$ and T. While it came out that the role played by temperature was considerable, strain

50

rate effect resulted to be weak for all materials investigated. For instance, the increase of ductility for OFHC copper, caused by T was of the order of 112% at 50% of homologous temperature while only an increase of 20%, approximately, for a strain rate of 10000 sec^{-1} was found. Since strain rates barely affect the strain to failure, it can be assumed that it has no effect on threshold strain as well.

The critical damage D_{cr} is related to the minimum net resisting section that can still sustain load in the reference volume element, prior failure. Once again, the experimental observations of Johnson and Cook confirm that the area at failure in specimen tested with Hopkinson bar, is scarcely sensitive to the strain rate while temperature has a higher effect.

More recently, Borvik et al. (1999) observed the same feature in a large number of tests performed on smooth and circumferentially notched tensile bar, i.e. different stress triaxiality conditions, see Figure 6.1

From these considerations, it is possible to suppose that strain rate affect all damage parameters in the same way. Thus following a correction for the set of damage parameters can be given as:

$$\begin{bmatrix} \tilde{\varepsilon}_{th} \\ \tilde{\varepsilon}_f \\ \tilde{D}_{cr} \end{bmatrix} = \begin{bmatrix} \varepsilon_{th} \\ \varepsilon_f \\ D_{cr} \end{bmatrix} \left(1 + C_1 \ln \frac{\dot{\varepsilon}}{\dot{\varepsilon}_0} \right) \tag{6.1}$$

where C_1 is a material constant, $\dot{\varepsilon}_0$ is a reference strain rate. ε_{th}, ε_f and D_{cr} are the quasi static damage parameters at room temperature.

7. DAMAGE MODEL: EXTENSION TO TEMPERATURE

If strain rate has a limited effect on material ductility, temperature has a more relevant effect that should be accurately quantified. The possibility to run direct damage measurements at high temperature is made difficult by the strict requirements that strain gauges and glue should satisfy: elevated cyclic deformation range (since ductility increases with temperature), durability, etc.

It is well known that temperature lowers material yield stress. This should have also an effect on the damage parameters. For instance, damage threshold strain, which is related to the strength of the bond between the ductile matrix and particle, should increase due to the weakening of the interface stresses similarly to the strain to failure.

Bonora and Milella proposed a correction for the material damage parameters as follow:

$$\begin{bmatrix} \tilde{\varepsilon}_{th} \\ \tilde{\varepsilon}_f \\ \tilde{D}_{cr} \end{bmatrix} = \begin{bmatrix} \varepsilon_{th} \\ \varepsilon_f \\ D_{cr} \end{bmatrix} \left(1 + \begin{bmatrix} A_1 \\ B_1 \\ C_1 \end{bmatrix} T^* \right) \tag{7.1}$$

51

where A_1, B_1, C_1 are material constants, T^* is the homologous temperature.

These constants have been determined estimated for low alloy steel, namely A533B, widely used in the nuclear industry. Material plastic flow at room and 100°C are given in Figure 7.1 and 7.2, respectively together with the damage parameter sets.
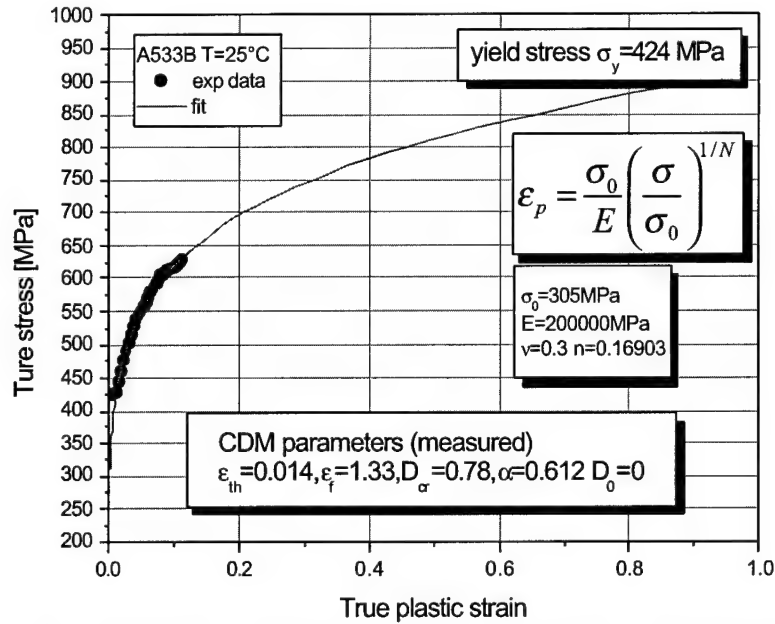

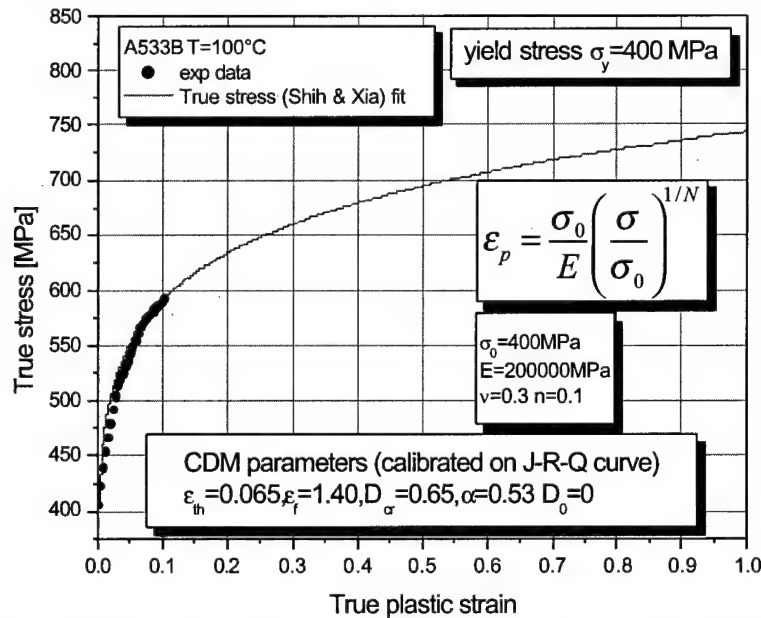*Figure 7.1 – Flow curve and CDM damage parameters for steel A533B @RT*

Figure 7.2 – Flow curve and CDM damage parameters for steel A533B @100°C

Here, the damage parameters at room temperature have been determined following the procedure indicated in Bonora (1999). The damage parameters at 100°C have been numerically derived over the crack resistance data at 100°C for a standard CT specimen, see Figure 7.3. Following the statement that damage parameters are a true material property, the corrected damage parameters set has been verified predicting material resistance curve in cracked geometry with different geometrical constraint.
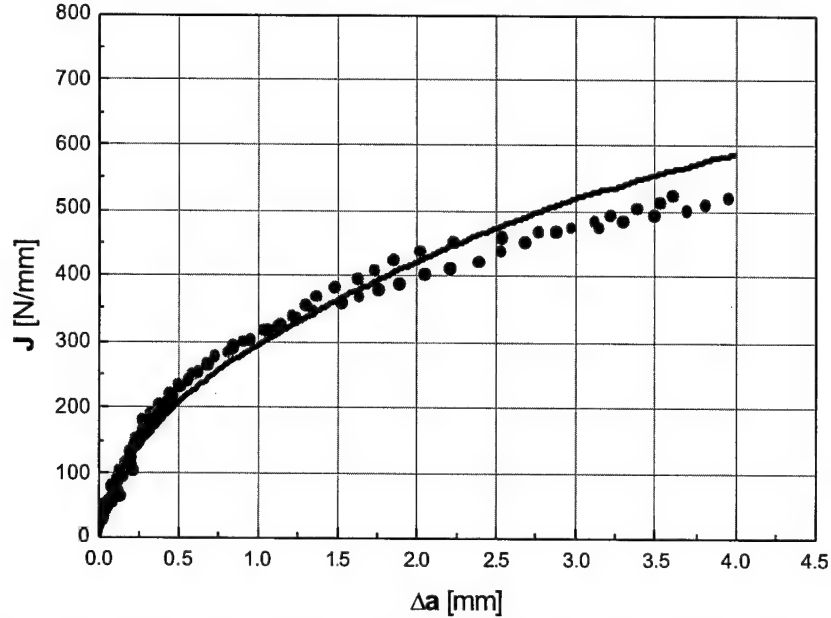

Figure 7.3 – Crack resistance curve for A533B steel at 100°C obtained on CT specimen configuration with a/W=0.62: damage parameters matching
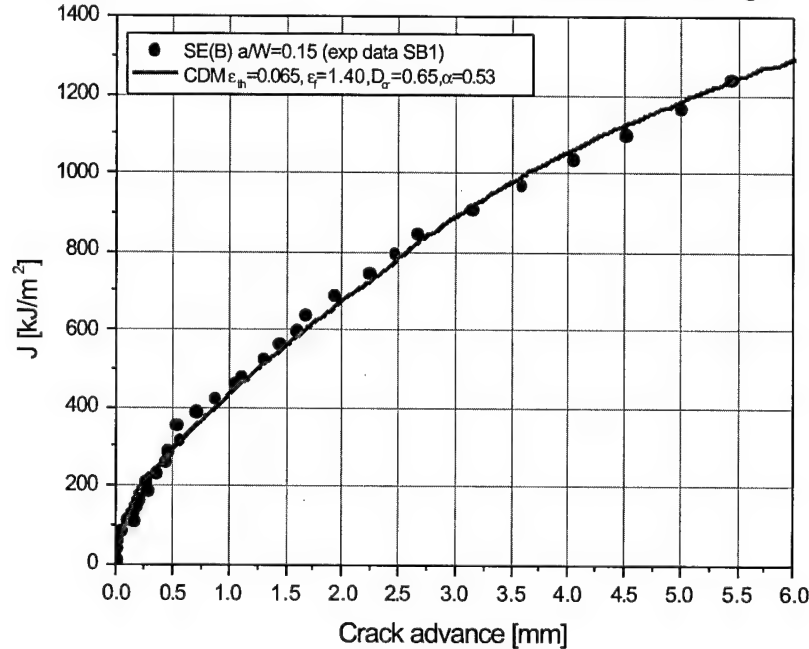

Figure 7.4 – Verification of damage parameters set. Prediction of crack resistance curve for A533B steel at 100°C on SE(B) specimen configuration with a/W=0.15

In table 7.1 the damage parameters sets for the two temperatures are summarized while in Figure 7.5 the comparison of the two corresponding damage curves is also give.

T	ε_{th}	ε_f	Dcr	α
25°C	0.014	1.3	0.78	0.61
100°C	0.065	1.4	0.65	0.53

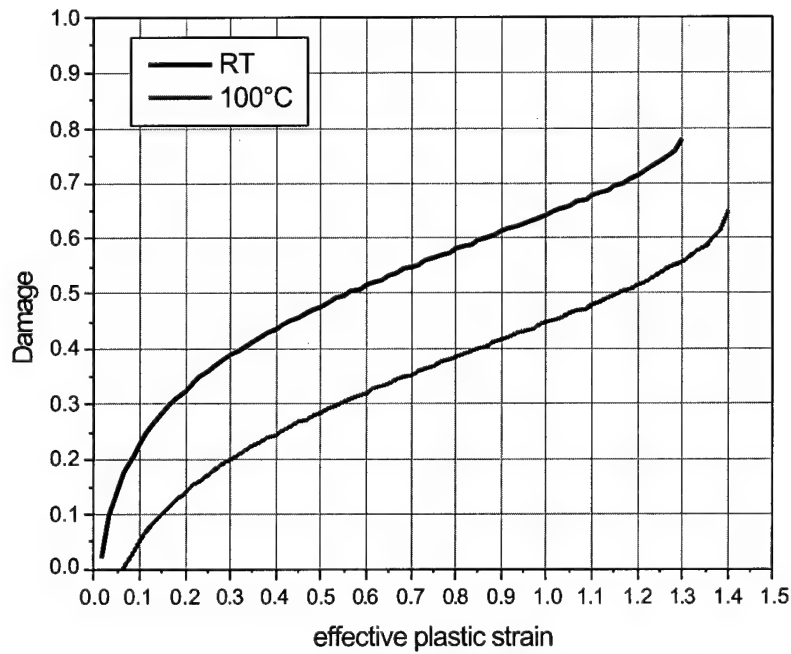*Table 1 – damage parameters for A533B steel*

Figure 7.5 – Damage evolution law at different temperatures

54

8. EXTENSION TO REVERSAL PLASTIC FLOW

Ductile damage formulations available in the literature always address tensile loading configuration, since it is well known that positive stress triaxiality enlarges nucleating voids in the material microstructure. The possible effect on damage variable due to compressive loading is usually neglected in the theoretical formulations.

The major consequence of this limitation is that the damage variable, D, has to be associated to the total effective accumulated plastic strain, usually indicated with p, that plays the role of the associated internal variable. In the literature, little attention is given to the effects on the material constants, or constitutive response, due to plastic deformation under pure compressive loading. This knowledge is critical in order to develop a predicting model capable to account for plastic strain reversal as for low cycle fatigue.

Few attempts based on the cyclic accumulation of damage, or its associated variable, always resulted in predicted very short lives as a consequence of the fact that p usually accumulates quickly. Porosity models, such as the Gurson model, are incapable to predict material failure since porosity effects are fully recovered during compressive loading resulting in a unrealistic healing-material behavior. These premises clearly indicate that additional hypotheses must be formulated in order to describe properly material behavior under compressive stress states. If ductile damage can be imputed to the formation and growth of microcavities that have the effect to reduce the net resisting area, and consequently material stiffness, thus the following scenarios can be speculated.

Scenario a). The material is initially stress-free and it is assumed that no strain history has modified its status from the one of "virgin material". Let us assume to start to load a material reference volume element, RVE, under pure compressive uniaxial state of stress avoiding any buckling phenomena. In this configuration, microvoids cannot nucleate since the ductile matrix is compressed around the brittle inclusions. If the local stress in the particle overcomes the particle strength, the particle itself can eventually break. This kind of damage should not affect material stiffness since no reduction of the net resisting area is occurred. The only effect that we would expect is probably an anticipated microvoids nucleation, due to an early void opening since the particle is broken, when the stress state is reversed in tension, (i.e. a lower strain threshold value). Even though an irreversible process such as particle breaking will eventually occur under compressive loads, the stiffness should remain unaffected indicating no damage in compression.

Scenario b). Let say that the virgin RVE is initially loaded in tension until some amount of damage. Then, the load is reversed in compression developing additional plastic strain. In this case, during the unloading from positive stress-state to zero, microvoids can close controlled by the large ductile matrix volume movement, (here, potential buckling of microcavities is neglected). Voids implode back to the particle from which they have nucleated. Void closure can eventually close to the zero displacement condition. During this phase the net resisting area is restored and the stiffness should be the same as for the virgin material. Continuing in the compressive ramp the stiffness,

once again, should remain unaffected. Further compressive loads, will eventually breaks some particles, but no effects are expected on E. A new reload in tension would see both the opening of the previously grown voids plus the opening of the new ones nucleated at the broken particles. However, at this stage it can be assumed that compressive damage does not modify damage developed under positive stress states.

It follows that ductile damage can accumulate under positive stress state only, while total plastic strain will accumulate under both. Consequently, the associate damaged variable has to be a redefined as an "active accumulated plastic strain" p^+, i.e. the plastic strain that accumulates if and only if, the actual stress triaxiality is greater than zero. Similarly, the damage effect on material stiffness will also be activated if and only if the current stress triaxiality is positive.

According to this, the damage model proposed by Bonora can be modified in terms of active damage D^+ and active plastic strain p^+ as follows:

$$\dot{D}^+ = -\dot{\lambda}\frac{\partial f_D}{\partial Y} = \alpha \cdot \frac{(D_{cr} - D_0)^{\frac{1}{\alpha}}}{\ln(\varepsilon_f / \varepsilon_{th})} \cdot f\left(\frac{\sigma_H}{\sigma_{eq}}\right) \cdot (D_{cr} - D^+)^{\frac{\alpha-1}{\alpha}} \cdot \frac{\dot{p}^+}{p^+} \tag{8.1}$$

$$\dot{p}^+ = \frac{\dot{\lambda}}{(1 - D^+)} H\langle f(\sigma_m / \sigma_{eq})\rangle \tag{8.2}$$

$$\tilde{E} = E(1 - D^+)H\langle f(\sigma_m / \sigma_{eq})\rangle \tag{8.3}$$

where

$$H\langle f(\sigma_m / \sigma_{eq})\rangle = \begin{cases} 0 & \sigma_m / \sigma_{eq} < 0 \\ 1 & \sigma_m / \sigma_{eq} \geq 0 \end{cases} \tag{8.4}$$

The model has been implemented into the commercial finite element code MSC/MARC through a number of user subroutines. Damage model performance under cycling loading has been firstly checked on a single axisymmetric 4 node element. The element size is 1.0 x 1.0 mm. The material is a 22NiMoCr37 steel of German production for which damage parameters were previously determined by Bonora. A cyclic imposed displacement with zero mean value $\delta_m=0$ and amplitude $\delta_a=0.2$ mm has been applied until element failure. Response under isotropic and kinematic hardening is given in Figure 8.1 together with the displacement evolution with time. Here, time is a fictitious variable since viscoplastic and time dependent behaviors have been neglected.

In Figure 8.1 it is shown how the effective plastic strain, together with active damage, accumulates only when stress triaxiality is positive. In this case, where the imposed nominal strain amplitude is 20%, failure is expected to occur after 5 cycles.
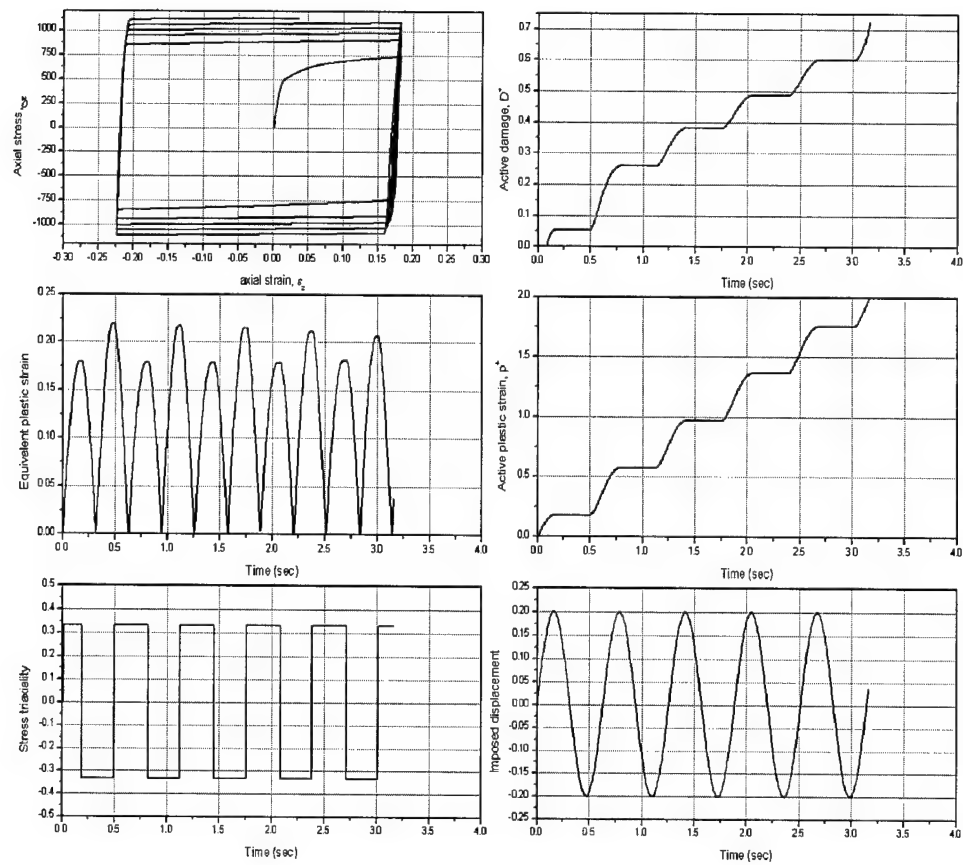
Figure 8.1 – Active damage and other variable evolution for a single element benchmark test

9. EXPERIMENTAL TESTING ON COPPER 99.9%

In addition to all other material data reported and discussed in this report, the attention has been focused on pure copper 99.9 that is of particular interest for AFOSR applications. A number of different tests have been performed in order to measure both constitutive response under controlled dynamic conditions together with to damage performance.

The material under investigation was a pure copper 99.9 (electrolytic) small grain hard worked (Copper FSH) and it is commercially available in plate form. A plate 900 x1000 x 15 mm thick has been bought and specimens have been machined.

Four different specimen geometries have been machined:

a) reduced size round tensile bar specimen
b) small size tensile bar specimen
c) hourglass flat specimen for damage measurements
d) micro charpy V notch

After machining, each specimen has been annihiled for 3h at 600°C in inert atmosphere. Dimension stability has been checked after heat treatment.

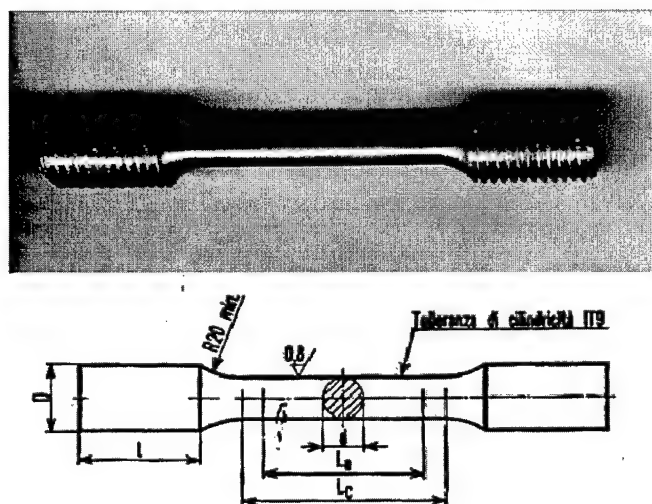In Figure 9.1.a-9.1c specimen dimensions and real pictures are given.

Figure 91.a – Round bar specimen for tensile loading: L_c=36 mm, L_D=6 mm
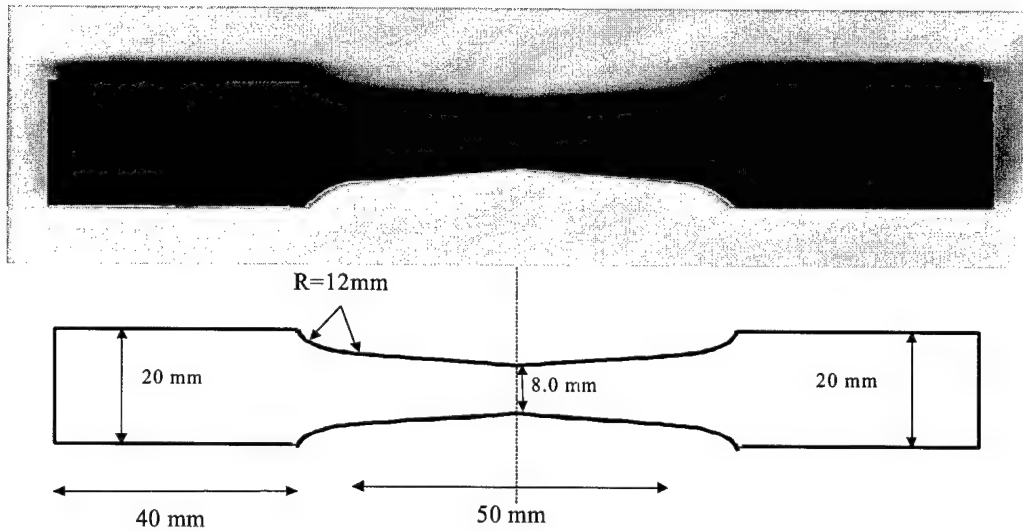
Figure 91.b – Hourglass rectangular flat bar specimen for damage measurements
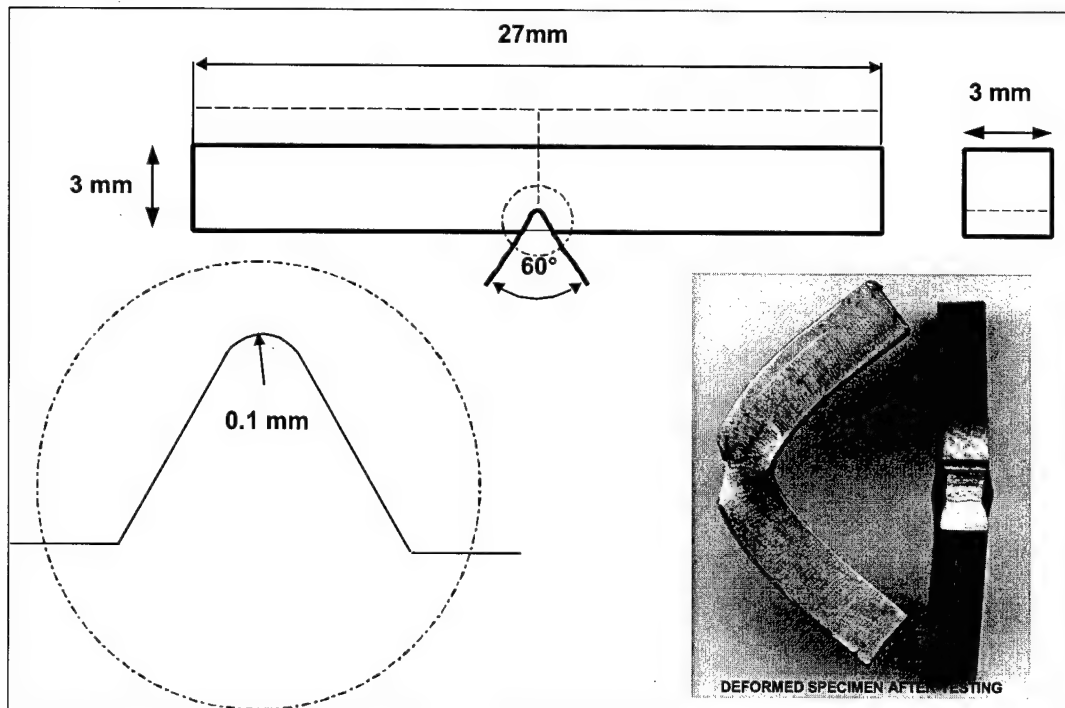

Figure 9.1.c – Microcharpy V notch specimen geometry and dimensions

Thermal treatment after machining plays a critical role on the material stress-strain response as given in figure 9.2. Here the large increase in the strain to failure can be observed.
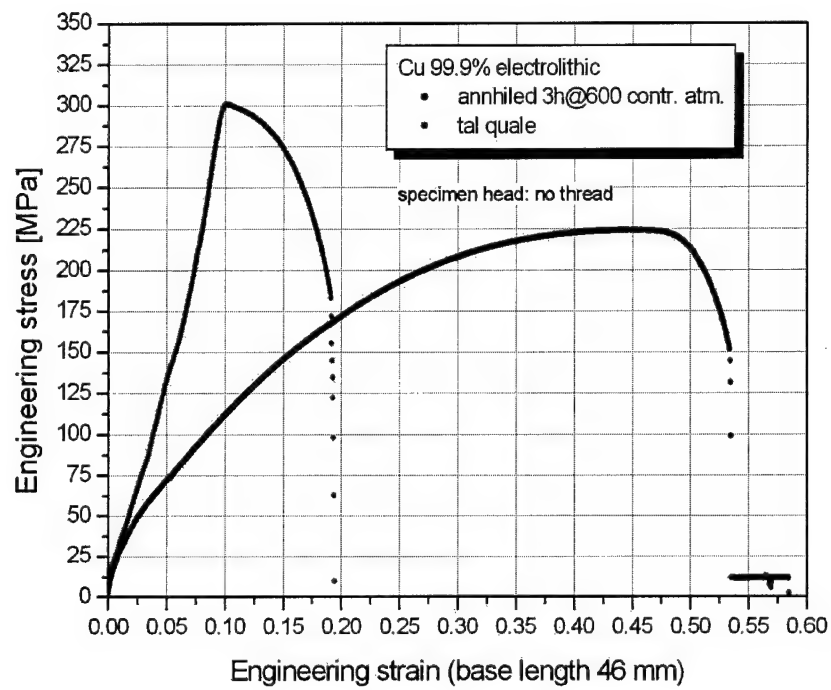
Figure 9.2 – Comparison of stress strain response for Cu 99.9 with and without heat treatment process.

10. DAMAGE MEASUREMENTS

The evolution of ductile damage variable under quasi-uniaxial state of stress conditions was measured using HG(T) specimen. The experimental procedure was organized in the following steps:

a) the specimen surface at the minimum section, where failure will occur by localization of plastic deformation, was cleaned and a strain gauge (3×6.2 mm) was positioned with the long side aligned with the axial direction using a two components epoxy glue. The strain gauge deformation limit was ±20.0% @120Ω.

b) the specimen was mounted on a MTS 100 KN hydrodynamic testing machine and a first loading ramp, imposing a remote displacement, was performed in order to recover machine and grip gaps;

c) a sequence of loading and unloading were performed progressively increasing the maximum strain. During this phase the applied load, together with the strain gauge deformation, were continuously monitored. In addition, a clip-gauge, with a reference length of 25.4 mm, positioned along the thickness and across the minimum section, was used to have a double-check measurement of the strain in the minimum section and information on the damage localization. Each unloading was used to verify the loss of stiffness due to damage. Since the specimen has not a constant section, the true stress in the minimum section is unknown. However, the knowledge of the actual stress is not needed for the damage evaluation since from Equation 2 the stiffness reduction is the only datum necessary. Thus, geometric stiffness given as the applied load by the actual strain can be used for a direct measure of damage. The loading-unloading process is repeated until the maximum strain allowable for the strain gauge is applied.

d) When the limit strain is reached, the strain gauge needs to be removed. Thus, the specimen was unloaded and a new strain gauge was positioned.

e) Before running new damage measurements, a loading ramp, below the previously reached maximum strain, was performed in order to verify eventual positioning errors.

Thus, the process, starting at the point b), can be repeated theoretically until complete failure of the specimen would occur. However, above a given strain level, as a result of the necking process that takes place in the minimum section, the positioning and balance of new strain gauges becomes impracticable.

This procedure, even if conceptually simple, is time consuming, since for a given loading rate the time required by any ramp becomes longer and longer. Attention must be paid since the entire measurement chain can be lost if the strain gauge deformation limit is accidentally exceeded. In addition, the replacement of the each strain gauge required a curing cycle of 3 hours at 50°C.

The glue itself can be a limit to the number of unloading ramps that can be performed since glues, that can sustain high deformations, usually show poor fatigue performance. The number of the measurements performed was good enough to fully identify the

damage parameters. Later, all specimens were loaded up to failure in order to provide the last damage data point through the measure of the effective resisting area at rupture. In Figure 10.1 the damage evolution law together with log-log plot for the identification of α exponent, Figure 10.2 are given.
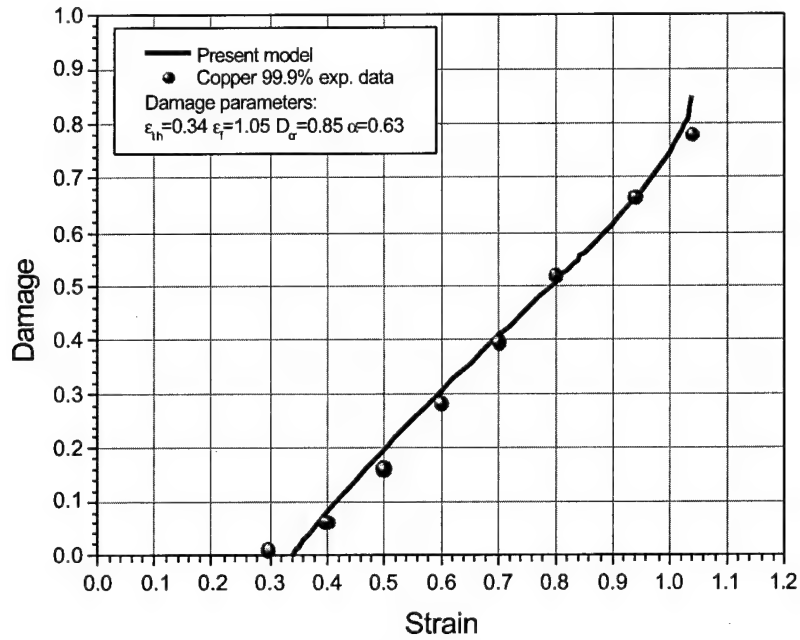

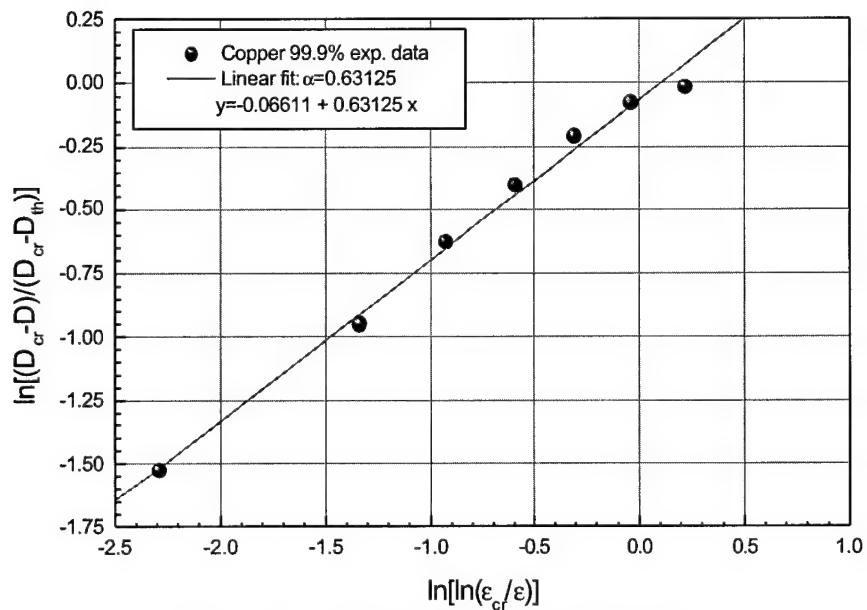*Figure 10.1 – Damage evolution in pure copper 99.9%*

Figure 10.2 – Damage exponent identification

11. CONCLUSIONS

The present study shows that the unified solid state equation (USSE) proposed, given by Eq. (2.5.1), is well predicting the evolution of the yield strength with both temperature and strain rate, of several BCC and HPC metals, as well. Figure 4.1 shows the overall picture for all metals considered in this study. It can be seen how experimental results (open or closed circles) are matched by the theoretical predictions (solid curves). Two
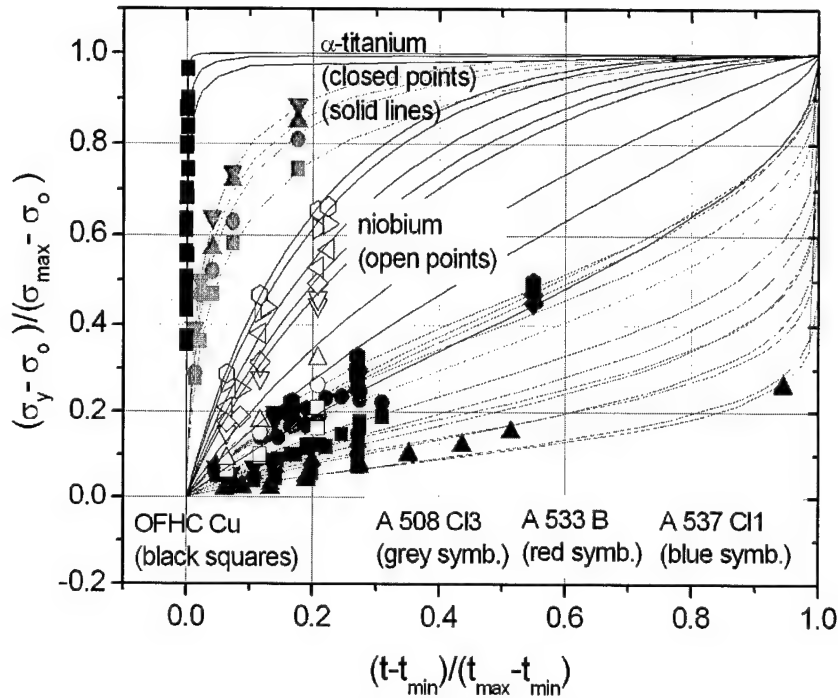

Figure 2.34 – Overall picture of the data analyzed in the present study.

typical behaviors can be distinguished: the first is related to strain rate exponents below 0.2-0.3 and is represented by concave lines, the second is characterized by m values larger than one and is represented by convex curves. In the first case, the metal response to temperature is slow and becomes larger and larger as the minimum temperature T_{min} is approached or, which is equivalent, as $(t-t_{min})/(t_{max}-t_{min})$ goes to one. This behavior is shown by BCC metals at low strain rates where, at temperatures not too low, diffusion rate are comparable with dislocation velocities. For carbon steels, a low strain rate is below 1000 - 500 s^{-1}, for niobium, instead, it is below 0.01 s^{-1}. Here temperature washes out the strain rate effect which can develop only at low temperatures. In the second case, the material response to dynamic loads saturates very fast with temperature, within the range $0 < (t-t_{min})/(t_{max}-t_{min}) < 0.2$. To this class of materials belong HCP metals and FCC ones. Particularly interesting appears to be OFHC copper, whose response with decreasing temperature saturates almost immediately. In between the two there are BCC metal behavior at larger strain rates. Niobium, in particular, will approach the HCP structure metals already at strain rates as low as 0.2 s^{-1}.

Damage model has been extended in order to account for compressive state of stress. This feature is of fundamental importance for all those applications where load history is complex, such as low cycle fatigue and dynamic impact.

The preliminary study performed on stress wave propagation in Charpy hammer seems to confirm the possibility to use this equipment as a dynamic testing machine to get quick and cheap information on dynamic material response.

12. REFERENCES

Bonora, N. and Newaz, M.G., (1998) "Low Cycle Fatigue Life Estimation for Ductile Metals Using a Non-Linear Continuum Damage Mechanics Model", Int. J. Solid and Stuctures, **35** , pp. 1881-1894.

Bonora, N., (1997) "A Non-Linear CDM Model for Ductile Failure", Engineering Fracture Mechanics, **58**, pp. 11-28

Bonora, N., (1998) " On the Effect of Triaxial State of Stress on Ductility Using Nonlinear CDM Model", Int. Journal. of Fracture, **88**, pp. 359-371

Bonora, N., (1999),"Ductile Damage Parameters Identification And Measurement", Journal of Strain Analysis, **34**, no 6, pp. 463-478.

Bonora, N., and Milella, P.P., (2001), "Constitutive Modeling For Ductile Metals Behavior Incorporating Strain Rate, Temperature And Damage Mechanics", to appear in International Journal of Impact Engineering.

Bonora. N., and Milella, P.P., (2000)," Strain Rate And Temperature Effect In Ductile Failure Process: Characterization And Modeling Using Continuum Damage Mechanics", AFOSR/AFRL SPC F61775-99-WE066, July 2000

Borvik, T., Langseth, M., Hopperstad, O.S., Malo, K.A., (1999), "Ballistic penetration of steel plates", Int. J. of Impact Engineering, **22**, pp.855-886

Campbell J.D., "Yield Delay Time of Mild Steel", Trans. ASM, 51, p.659, 1959

Campbell J.D.,"The Dynamic Yielding of Mild Steel", Acta Metall., 1, p. 706, 1953

Conrad H., "On the Mechanism of Yielding and Flow in Iron", Jour. Iron Steel Inst., 198, p. 364, 1961

Conrad H., Hayes W., "Correlation of the Thermal Component of the Yield Stress of the BCC Metals", Aerosp. Corp., 1962

Conrad H., Wiedersich H., "Activation Energy for Deformation of Metals at Low Temperatures", Acta Metall., 8, p. 128, 1960

Cottrell A.H., " Effects of Solute Atoms on the Behaviour of Dislocations", Ph. Soc., p. 30, 1948

Cottrell A.H., "Deformation of Solids at High rates of Strain", Conf. on Prop. of Mat. at High Rates of Strain, pp. 1-12, 1957

Cottrell A.H., "Dislocations and Plastic Flow in Cristals", Oxford, 1953

Cottrell A.H., Bilby B.A., "Dislocation Theory of Yielding and Strain Aging of Iron", Ph. Soc., 62, p. 49, 1949

Cottrell A.H., Theory of Brittle Fracture in Steels and Similar Metals", Trans. AIME, 212, pp. 192-203, 1958

Follansbee P.S., and Kocks U.F., Acta Metallurgica, Vol. 36, p. 81, 1988

Follansbee P.S., and Weertman, J, "On the Question of Flow Stress at High Strain Rates Controlled by Dislocation Viscous Flow", Mech. Mater., Vol. 1, pp. 345-350, 1982

Follansbee P.S., in Metallurgical Applications of Shock-Waves and High Strain Rate Phenomena, eds. L.E. Murr, K.P. Staudhammer, and M.A. Meyers, Dekker, New York, p.451, 1986

Gorman, J.A., Wood, D.S., and Wreeland, T. Jr., Journal of Applied Physics, Vol. 40, p.833, 1969

Granato, A.V., Metallurgical Effects at High Strain Rates, AIME Proceedings, p. 255, Eds. R.W. Rohde, B.M. Butcher, and C.H. Karnes, Plenum, New York, 1973

Gurson, A.L., (1977), "Continuum Theory of Ductile Rupture by Void Nucleation and Growth: Part I- Yield Criteria and Flow Rules for Porous Ductile Media", J. Engn. Mat. Tech., **99**, pp. 2-15

Hoge K.G., and Mukherjee A.K., Jou. Mater. Sci., Vol. 12, p. 1666, 1977

Hollomon J. H., "The Mechanical Equation of State", Trans. AIME, 171, pp. 535-545, 1947

Johnson G.R. and Cook W.H., Proc. 7th Inter. Symp. Ballistic, Am. Def. Prep. Org. (ADPA), Netherlands, 1983

Johnson G.R., Hoegfeldt J.M., Lindolm U.S., and Nagy A., (1983), ASME Jour. Eng. Mater. Tech., Vol. 105, p. 42

Johnson G.R., Hoegfeldt J.M., Lindolm U.S., and Nagy A., ASME Jour. Eng. Mater. Tech., Vol. 105, p. 42, 1983

Kanninen M. F. et al., NUREG CR/4219, Vol. 4, No. 2, 1987

Kapoor, R., Nemat-Nasser, S., „Comparison between High Strain Rate and Low Strain Rate Deformation in Tantalum", Materials Transactions, 1999.

Klopp R.W., Clifton R.J., and Shawki T.G., Mech. Mater. , Vol 4, p. 633, 1985

Lemaitre, J.,(1985), "A continuous damage mechanics model for ductile fracture", J. of Engng. Mat. and Tech., **107**, pp. 83-89

Manjoine M.J., " Influence of Rate of Strain and Temperature on Yield Stress of Mild Steels", Jour. Appl. Mech., 11, 4, A211-218, 1984

McClintock, F.A., (1968),"A criterion for ductile fracture by the growth of holes", J. Appl. Mech., **35**, pp. 363-371

Meyers, M.A., and Chawla, M.M., Mechanical Metallurgy, Principles and Applications, p. 304, fig. 8.9, Prentice-Hall, 1984

Meyers, M.A., and Murr, L.E., "Defect Generation in Shock-Wave Deformation", Shock Waves and High Strain-Rate Phenomena in Materials, Ed. M.A. Meyers and L.E. Murr, p. 502, Plenum Press,1981

Milella P.P., "Effetto della Temperatura e del Rateo di Applicazione della Deformazione sulla Tensione di Snervamento dei Metalli a Struttura CCC", In Italian, Italian Group of Fracture, 13th Symposium, Cassino, pp.34-43, 1997

Milella P.P., "Temperature and Strain Rate Dependence of Mechanical Behavior of Body-Centered Cubic Structure Materials", Paper presented at TMS Fall Meeting '98, Chicago, Illinois, 11-15 October 1998, to be published .

Milella P.P., "Temperature and Strain Rate Dependence of Mechanical Behavior of Body-Centered Cubic Structure Materials: further Developments", Invited Lecturer, Wayne State University, Detroit, Michigan, March 5, 1999.

Nemat-Nasser S., and Li Y., Acta Met. Mater. , Vol. 46, No. 2, p. 565, 1998a

Nemat-Nasser S., and Obata M., Proc. Royal Society of London, Vol. A407, p. 343, 1986

Nemat-Nasser S.,Okinaka T., and Ni L., J. Mech. Solids, Vol. 46, No 6, p. 1038, 1998b

Orowan E., "Dislocations and Mechanical Properties", Disl. in Metals, AIME, 1954

Petch N.J., "The Cleavage Strength of Policrystals", Jour. Iron Steel Inst., 174, p.25, 1953

Petch N.J., "The Fracture of Metals", Progr. in Metal Phys., 5, p.1, 1964

Petch N.J., Helsop J., "The Stress to move a Free Dislocation in Alpha Iron", Phil. Magaz., 47, p.886, 1956

Ping, Wang-Ze, (1994), "Void growth and compaction relations for ductile porous materials under intense dynamic general loading conditions, International Journal of Solids and Structures", 31, no. 15, pp. 2139-2150

Regazzoni, G., Kocks, U.F., Follansbee, P.S., "Dislocations Kinetics at High Strain Rates", Acta Metallurgica, Vol. 9, pp. 382-384, 1961

Seeger A., "The Generation of Lattice Defects by Moving Dislocations and Its Applications to Temperature Dependence of the Flow Stress in FCC Crystals", Phil. Magaz., 46, p. 1194, 1955

Seeger A., "The Temperature Dependence of the Critical Shear Stress and of Work Hardening of Metal Crystals", Phil. Magaz., 45, p. 771, 1954

Takeuchi; T., Journal of Physics Society Japan, Vol. 21, p.2616, 1966

Vohringer, O., Deformation Behavior of Metallic Materials, Ed. C.Y. Chiem, International Summer School on Dynamic Behavior of Materials, ENSM, Nantes, September 11-15, 1989

Wert C.A., Trans. AIME, 188, p.1242, 1950

Yokobori T., "The Cottrell Bilby Theory of Yielding of Iron", Ph. Rev., 88, p. 1423, 1953

Zener C., Hollomon J.H., " Effect of Strain Rate upon Plastic Flow", Jou. Appl. Ph., 15, 22-32, 1944.

Zerilli F. J., Armstrong R.W., Acta Met. Mat., Vol. 40, p. 1803, 1992

Zerilli F. J., Armstrong R.W., Jour. Appl. Phys., Vol. 61, p. 1816, 1987

Zerilli F. J., Armstrong R.W., Jour. Appl. Phys., Vol. 68, p. 1580, 1990